Automated Raman cytology system for cancer diagnostics

by

SHU YU WU

Submitted to the Department of Electrical Engineering
in partial fulfillment of the requirements for the degree of

Master of Engineering in Electronic Engineering

at the

NATIONAL UNIVERSITY OF IRELAND MAYNOOTH

October 2014

Author .....
Department of Electrical Engineering
October 15, 2014

Certified by .....
Bryan Hennelly
Research Fellow, Member of the Department of Electronic Engineering
and the Callan Institute,National University of Ireland Maynooth
Thesis Supervisor

Accepted by .....
Hugh Byrne
Head of Focas Research Institute,DIT

Automated Raman cytology system for cancer diagnostics

by

SHU YU WU

Submitted to the Department of Electrical Engineering
on October 15, 2014, in partial fulfillment of the
requirements for the degree of
Master of Engineering in Electronic Engineering

Abstract

Raman spectroscopy is a promising optical diagnostic tool that can be applied to unstained cells in order to detect changes in molecular composition. The data collected can be described as a chemical fingerprint of the sample under investigation. Thus it is very popular in the recent times to use Raman spectroscopy in cytology to increase diagnostic sensitivity and specificity for early stage cancer. In this thesis, I introduce an automated Raman cytology system for cancer diagnostics which integrates all the hardware and software in Micro-manager and operates them in a specific order. An autofocus algorithm for unstained cells and a three-dimensional morphology recovery algorithm are also investigated and contributed to the final automated system. With increasing usage of Raman cytology systems, automation is a solution to limit data variabilities which is a major problem at the moment. In addition, a higher throughput of cellular analysis and a reduction in manpower could be expected from the proposed automation system.

Thesis Supervisor: Bryan Hennelly
Title: Research Fellow, Member of the Department of Electronic Engineering and the Callan Institute,National University of Ireland Maynooth

Acknowledgments

I would like to express my gratitude to my supervisor, Dr. Bryan Hennelly, whose expertise, understanding, and patience, added considerably to my research experience.

A very special thanks goes out to Dr. Stephen Brown. He has been offering me working opportunities for the past year to partially support my research master and interesting research experiences in wireless sensor network field.

I must also acknowledge Dr. Nazim Dugan, Xin Fan, Laura Kerr and Sinead Barton for their kind cooperation and help both in academic and social aspects.

I would also like to thank my family for the financial and emotional supports. Without them I won't be able to have this incredible opportunity and experience in Maynooth University.

Contents

List of Figures

List of Tables

List of Contributions:

Published papers

- Shuyu Wu, Nazim Dugan, Bryan M. Hennelly, "Investigation of autofocus algorithms for brightfield microscopy of unstained cells", in Optical Modelling and Design III, Frank Wyrowski; John T. Sheridan; Jani Tervo; Youri Meuret, Editors, Proceedings of SPIE Vol. 9131 (SPIE, Bellingham, WA 2014), 91310T, presented in Brussels in Apr. 2014.

Journal papers in preparation

- Shuyu Wu, Nazim Dugan, Bryan M. Hennelly, "Recovery of three dimensional cellular morphology using brightfield microscopy", to be submitted to Jounral of Biomedical Optics 2014.

- Shuyu Wu, Xin Fan, Nazim Dugan, Bryan M. Hennelly, "Automated confocal Raman Micro-spectroscopy system for cellular analysis and cytopathology", to be submitted to Analyst 2014.

Posters

- Shuyu Wu, Nazim Dugan, Bryan M. Hennelly, "Fast recovery of 3D cell morphology from unstained cells using brightfield microscopy", presented at the Biophotonics and Imaging Graduate Summer School in National University of Ireland Galway in Jun. 2014.

Chapter 1

Introduction

Raman spectroscopy[1] is based on the inelastic scattering of monochromatic light, wherein the wavelength of the scattered photons is shifted by an amount dependent on the molecular properties of the sample[2]. Raman spectroscopy is particularly suitable for applications in biology because water is a weak Raman scatterer[3]. The increasing availability of high power lasers with narrow linewidth, and high quality filters that attenuate the Rayleigh scattered light, has led to a significant increase in the application of Raman spectroscopy in biology in recent years[4]. For biological samples that consist of a complex mixture of various biochemicals, the Raman spectrum can be used for fingerprint like identification. Although the spectra obtained from healthy and diseased tissue types can appear to be very similar, the use of multivariate statistical algorithms[5] can be applied in order to classify an unknown sample. This requires the recording of datasets of spectra belonging to known groups, which in turn enables the training of algorithms to achieve high diagnostic sensitivities and specificities[6]. In recent years the method has been demonstrated to be useful in diagnosing a range of different conditions including brain metastases[7], prostate[8], breast[9], esophagus[10], skin[11], bladder[12], oral[13], cervical[14] and lung[15] cancers.

This thesis is concerned with the application of Raman spectroscopy to cytology[16], i.e. to the investigation of cells and in particular for the identification of cancerous cells. This technique involves the integration of a Raman spectrometer into a stan-

dard clinical microscope and has become known as Raman micro-spectroscopy. The microscope objective serves to both deliver the source laser to a microscopic point on the sample and to collect the Raman scattered photons, while simultaneously allowing the microscope to image the sample. It is possible to obtain low noise spectra by employing a confocal aperture which serves to isolate the collected spectrum from a specific three dimensional point on the sample. Numerous companies offer high quality commercial Raman micro-spectrometers, such as Horiba and Renishaw, that are routinely employed in the analysis of cells and tissue samples[17].

The most common example of diagnostic cytology is the evaluation of cervical smears referred to as the Pap smear[18]. Cervical cytology is based on the qualitative inspection of images obtained under a microscope and requires a trained histopathogist. Recently it has been shown that confocal Raman micro-spectroscopy coupled with principal component analysis-linear discriminant analysis (PCA-LDA) modelling yielded a diagnostic accuracy of 84.1% (a sensitivity of 81.0% and a specificity of 87.1%) for in-vivo discrimination of dysplastic cervix[19]. The technique can be applied to cervical cells as a straightforward adjunct to the existing pap smear test and requires no further additional patient interaction. Bladder cytology is another area that has been shown to benefit from Raman micro-spectroscopy. Bladder cytology, whereby a histopathogist inspects epithelial cells shed into urine samples, can provide 80% to 90% sensitivity and 98% to 100% specificity for high grade samples[20] but only 20%-50% sensitivity for low grade samples[21] which make up the majority of cases. As a result, tissue biopsies are required as a standard. In the first patient study, Raman micro-spectroscopy has been shown to successfully diagnose between normal, low-grade and high-grade bladder cells with a sensitivity of 92% and specificity of 91%[12][22]. This discovery may pave the way for a completely non-invasive bladder cancer test.

Clearly, Raman micro-spectroscopy applied to cells (or Raman cytology for short) has potential to become a standard clinical diagnostic tool. However, some problems exist with the implementation of the technique in a clinical environment. Firstly, the cells cannot be stained before recording the spectrum because the additional chemicals

corrupt the recorded spectrum and may give rise to either fluorescence or photo-damage, which makes imaging difficult. The optimum location from which to obtain a Raman spectrum is the cell nucleus, but the location of the nucleus of an unstained cell is often challenging to identify. Once identified, the cell nucleus is aligned with the laser spot using a manually controlled translation stage and a spectrum is recorded for approximately 30 seconds. In many cases, improper alignment of the cell in one of the three dimensions results in a spectrum of poor quality and the cell must be realigned and the spectrum rerecorded. This is then repeated for a large number of cells and even for one patient sample, the overall process can be tedious and time consuming. The correct use of the system requires training and experience and the results obtained can vary from user to user due to slight variability in experimental procedures which reduces the reliability of the method. Standardisation of the approach is necessary in terms of equipment, consumables and methodologies if it is ever to be adopted a standard everyday clinical tool.

One significant step towards standardisation of Raman cytology is the automation of the overall process, and it is this subject that is addressed in this thesis. The obvious benefits of automation include reduced manual workload, faster turnover, and more reproducible and reliable results. However, an core challenge in full automation of Raman cytology is accurately targeting the unstained cell nucleus and getting the nucleus in-focus. Recently, an image processing method was outlined[23] that can identify the nucleus in an unstained cell using a segmentation algorithm based on fuzzy logic and it was proposed that this algorithm could potentially be utilised to develop an automated Raman cytology system. In this thesis, an automated Raman cytology system based on an novel image processing algorithm is proposed that can quickly identify the nucleus of an unstained cell. This is realised by recording images of slightly out of focus planes in which the nucleus effectively behaves like a small lens to produce a tightly focused bright spot which indicate the location of nucleus. Another sophisticated nucleus targeting algorithm is also investigated in this thesis for the purpose of accurately targeting, which is termed unstained cell morphology recovery algorithm. The cell morphology is achieved by applying a new autofocus

algorithm for unstained cell recording by bright-field microscope on different parts of the image.

The main contribution of this thesis is the development of a fully automatic Raman cytology. This proposing method is built around Micro-manager[24], an open source software package for the control of microscope related hardware. A large area of a slide is scanned, and candidate cells are identified using image processing algorithms; these cells are ordered according to a quality metric applied to the images of the bright spots. Following this, the selected cells are sequentially aligned in three dimensions with the laser spot and spectra are recorded. A clear description of the process is provided such that it may be implemented by anyone using a commercial Raman micro-spectrometer or a custom built set-up. All of the software employed to control the various hardware in the system (digital camera, translations stage, filter wheel, spectrograph, microscope lamp, spectrograph and cooled CCD) is open source and freely available. The method outlined in this thesis may pave the way for fully automated Raman diagnostics that can be used for mass screening of oral, cervical and bladder cancer.

The breakdown of this thesis is as follow; In Chapter 2, 15 autofocus metrics are investigated for unstained cells recorded by brightfield microscopy. The main difference in the behaviour of autofocus metrics applied to opaque objects and unstained transparent cells are emphasized and illustrated. The optimum metrics are identified in this chapter and are applied in the following chapters in order to find the focal plane of a region or the global image. In Chapter 3, the best performing metrics selected from chapter 2 are further investigated for different parts of the cell image in order to recover a depth map of the cell and in this way estimate the 3D morphology of unstained cells. Two methods are proposed; the first provides low resolution depth maps but can be performed quickly while the second provides high resolution depth maps but is computationally slow. Chapter 4 provides a detailed explanation of the proposing automated Raman cytology system both in terms of hardware and software.

Chapter 2

Investigation of autofocus algorithms for bright-field microscopy of unstained cells

In the past decade, there has been significant interest in image processing for bright-field cell microscopy because the additional chemicals will corrupt the spectrum and may give rise to either fluorescence or photo-damage. For some applications, where the biochemical integrity of the cell is required to remain unchanged so that sensitive chemical testing can later be applied, it is necessary to avoid staining. In particular, Raman spectroscopy and Raman cytology can only be applied to unstained cells recorded by brightfield microscope. Much of the previous research on image processing for microscopy has focused on fluorescence microscopy, including cell counting, cell tracking, cell segmentation and autofocusing. Fluorescence microscopy provides functional image information that involves the use of labels in the form of chemical stains or dyes. Unstained cells are often effectively transparent and appear to have a homogeneous intensity profile when they are in focus. Brightfield microscopy is the most universally available and most widely used form of optical microscopy and for the various reasons already mentioned it is interesting to investigate image processing of unstained cells recorded using a standard bright field microscope. In this chapter, the application of a range of different autofocus metrics applied to unstained bladder

cancer cell lines using a standard inverted brightfield microscope with microscope objectives that have high magnification and numerical aperture are investigated. A number of conclusions on the optimum metrics and the manner in which they should be applied for this application are presented.

The brightfield microscope is the most common form of microscope and has played an essential role in clinical science for over a century[25]. It is comprised of a white light source, usually a halogen lamp, which is focused onto a sample using a condenser lens. The light passes through a partially transparent sample and into a microscope objective. The sample plane is imaged to a digital camera and/or a set of oculars via the microscopic objective. Variations in the absorption of the sample contribute to the image that is recorded by the camera. Only objects that have the property of absorbing light can be imaged to the camera plane. In many cases cells or other biological samples can appear to be effectively transparent and the resulting brightfield microscopic image can appear to contain very little contrast. To compensate for this, staining is often employed in order to add absorption to parts of the sample, eg, the nucleus of a cell. While this facilities imaging using the brightfield microscope, it has the disadvantage of being time consuming, costly and in many cases the dyes can be toxic to the cells, and therefore the cells must first be fixed before imaging.

The inability of brightfield microscopy to image unstained transparent cells has resulted in the development of other forms of microscopy. Phase contrast microscopy[26] and digital holographic microscopy,[27][28] both enable variation in the refractive index and/or thickness of the sample to be measured, which allows for visualization of the cell, and the cell nucleus without the need for staining. However, phase contrast requires the use of specially designed microscope objectives and digital holographic microscopy requires a laser and expensive optical elements. Differential Interference Contrast (DIC) microscopy[29] offers a significant improvement in contrast for unstained cells. This technique uses a series of Wollaston prisms and polarisers, both before the condenser and after the microscope objective, the purpose of which are to split the illuminating light into two slightly misaligned light sources which are then realigned after passing through the sample. The effect is to create an interference pat-

tern that highlight subtle changes in the path lengths travelled and thereby provide high contrast of features in the object. The main disadvantage of DIC microscopy is the expense of the additional optical elements and suitable microscopy objectives.

Fluorescence microscopy[30] involves the use of fluorescent labels or fluorophores that can bind to a specific part of the cell where they absorb a specific wavelength and emit light of longer wavelength. The location and the amount of the label can be observed in the image and this can reveal functional information about a particular part of a cellular structure or a process. Fluorescence microscopy is often expensive; it normally requires a monochromatic source such as a laser as well as dichroic mirror, a filter and a suitable low noise camera. In some cases, fluorescence microscopy cannot be used due to inherent cell damage caused by phototoxicity[31]. Often multiple fluorescent channels are required to image different parts of the cell such as the nucleus and the cytoplasm and this can increase the expense and experimental difficulty[32].

Despite the advantages afforded by the various microscopy techniques discussed above, brightfield microscopy remains the most ubiquitous, inexpensive and widely used form of microscopy and is the prevalent form of microscopy applied in Raman micro-spectroscopy. To date a range of image processing techniques have been developed for microscopy but many of these focus on applications involving digital holographic microscopy,[28][32] or fluorescence microscopy.[30][33] In the past decade, there has been increasing attention on image processing algorithms for brightfield microscopy in order to enhance the overall functionality of the technique, particularly for imaging transparent unstained cells.[34][35][36][37][38][39][40][41] Many of these papers discuss algorithms that have been shown to successfully calculate the cell boundary and the cell nucleus for transparent unstained cells that have been recorded using brightfield microscopy. In particular level set contouring has been shown to successfully segment unstained cells[38]. Some of these algorithms make use of the fact that, when the cell is slightly out of focus, certain cell information is revealed that can be used to segment the cell.

Despite the recent interest in image processing of unstained cells, to the best of my knowledge, there has been no comprehensive investigation of autofocusing of un-

stained cells and it is this subject which is explored in this chapter. While it has been acknowledged that autofocusing has a long history in microscopy.[42][43] Investigations to date have focused on objects that absorb light. Autofocusing algorithms generally require the recording of a stack of images for a range of distances where the object is moved relative to the microscope objective. A metric is then applied to each image in the stack and the image which results in this metric having a maximum value is taken to be the most in focus image. These metrics are universally based on the idea that, when the image is in focus, image detail can be observed and so they often quantify the amount of high frequency content or variation in the image. However, for the case of objects which appear to have a homogeneous intensity pattern, such as transparent cells, it is well known that these metrics fail. In this chapter, the application of 15 well known autofocusing metrics to unstained cells are investigated and the behaviour of these metrics are compared with that obtained from an abosorbant object, also recorded using brightfield microscopy. How these metrics can be adapted to work for transparent cells is demonstrated and the metrics provide the best results are determined.

The breakdown for this chapter is as follow; In Section 2.1, the various autofocus metrics that are investigated for this thesis are introduced. In Section 2.2, the difference in the behaviour of these metrics are analysed for transparent cells and opaque objects. To do this, all 15 metrics are applied on stacks of unstained bladder cancer cell images and a USAF resolution chart. By evaluating the performance of these metrics conclusions are made on how these metrics can be adapted for transparent objects and three of the best performing metrics are selected for further study. The three selected metrics are applied on a cheek cell, a blast cell and a bladder cancer cell respectively in Section 2.3 to prove the robustness of the method. The work presented in this chapter has been published in a recent conference proceedings[44].

2.1 Autofocus Metrics

In this section, the various theoretical aspects of traditional autofocusing are introduced and a number of commonly used metrics that are utilised at the core of autofocusing algorithms are briefly overviewed. In this chapter the application of these various metrics are investigated for the autofocusing of unstained epithelial cells obtained using standard brightfield microscopy. The transparent nature of these cells means that these metrics cannot be employed in a traditional sense and further investigation is required. The manner in which focus curves are computed and analysed for these transparent cells is explained step by step in Section 2.2. In addition, the difference between the focus curves that are calculated for transparent and opaque cells is emphasised in Section 2.2.

In order to realize autofocusing the use of a focus metric is required that can be applied to a stack of images by comparing this metric across each image in the stack. It is possible to identify the most 'in-focus' image by examining the behaviour of this metric across the set of images. In this chapter, 15 different autofocus metrics listed below are investigated. While these metrics have previously been applied to opaque images,[42] to the best of my knowledge, this chapter represents the first investigation of these algorithms applied to images of transparent unstained cells, obtained using brightfield microscopy. The metrics are as following;

1. Absolute Gradient:

$$f(n_z) = \frac{1}{N_x N_y} \sum_{n_x=0}^{N_x-1} \sum_{n_y=0}^{N_y-1} \left| I\left(n_x\Delta_x, n_y\Delta_y, n_z\Delta_z\right) - I\left(n_x\Delta_x, n_y - 1\Delta_y, n_z\Delta_z\right)\right| \quad (2.1)$$

Where I represents the digital image recorded by a digital camera; Δ_x and Δ_y represent the camera pixel size in the x and y directions respectively and Δ_z is the distance the stage is moved between the capture of subsequent images in the vertical direction; n_x and n_y take the range of 0 to N_x - 1 and 0 to N_y - 1 where N_x and N_y are the number of pixels in the x and y directions respectively and n_z takes the range of 0 to N_z -1 where N_z is the total number of images recorded. For the sake of brevity the

above equation is rewrote where the Δ_x, Δ_y and Δ_z parameters are omitted:

$$f(n_z) = \frac{1}{N_x N_y} \sum_{n_x=0}^{N_x-1} \sum_{n_y=0}^{N_y-1} |I(n_x, n_y, n_z) - I(n_x, n_y - 1, n_z)| \tag{2.2}$$

This notation is employed for the remainder of this thesis.

2. Square Gradient:

$$f(n_z) = \frac{1}{N_x N_y} \sum_{n_x=0}^{N_x-1} \sum_{n_y=0}^{N_y-1} [I(n_x, n_y, n_z) - I(n_x, n_y - 1, n_z)]^2 \tag{2.3}$$

The two metrics given above in Eqn(2.2) and Eqn(2.3) are related to the gradient of the image. In image processing, the gradient represents the rate of change of the image in a given direction. For a non-transparent image that is in-focus and therefore contains high frequency detail, the magnitude of the gradient (the difference between the grey-scale values of a pixel with its' horizontal neighbour) will be larger than the magnitude of the gradient for out-of-focus images.

3. Netten's Filter[45]:

$$f(n_z) = \frac{1}{N_x N_y} \sum_{n_x=0}^{N_x-1} \sum_{n_y=0}^{N_y-1} [I(n_x + 1, n_y, n_z) - I(n_x - 1, n_y, n_z)]^2 \tag{2.4}$$

This metric is similar to the previous two metrics and compares the difference in grey-scale values between neighbours along the vertical direction.

4. Energy Laplace:

$$f(n_z) = \frac{1}{N_x N_y} \sum_{n_x=0}^{N_x-1} \sum_{n_y=0}^{N_y-1} [A(n_x, n_y, n_z)]^2 \tag{2.5}$$

$$A(n_z) = I(n_z) * \begin{bmatrix} -1 & -4 & -1 \\ -4 & 20 & -4 \\ -1 & -4 & -1 \end{bmatrix} \tag{2.6}$$

This metric makes use of the discrete convolution of the image with the Laplace mask, shown above in Equ(2.6), to compute the second derivative $A(n_z)$. The value of $f(n_z)$

is given by the sum of the squares of the result of this convolution.

5. Laplacian:

$$f(n_z) = \frac{1}{N_x N_y} \sum_{n_x=0}^{N_x-1} \sum_{n_y=0}^{N_y-1} \left[I\left(n_x, n_y - 1, n_z\right) - 2I\left(n_x, n_y, n_z\right) + I\left(n_x, n_y + 1, n_z\right) \right]^2 \quad (2.7)$$

This metric is based on the sum over the image of the squared second derivatives and has been previously used by Muller and Buffington[46]. In the Fourier domain, the transfer function of a second order difference filter (Laplacian) enhances the higher spatial frequencies more strongly than the first-order difference filter (Gradient)[47].

6. Tenenbaum gradient:[48][49]

$$f(n_z) = \frac{1}{N_x N_y} \sum_{n_x=0}^{N_x-1} \sum_{n_y=0}^{N_y-1} \left[T_x\left(n_x, n_y, n_z\right) \right]^2 \left[T_y\left(n_x, n_y, n_z\right) \right]^2 \quad (2.8)$$

$$T_x(n_z) = I(n_z) * \begin{bmatrix} 1 & 2 & 1 \\ 0 & 0 & 0 \\ -1 & -2 & -1 \end{bmatrix} \quad (2.9)$$

$$T_y(n_z) = I(n_z) * \begin{bmatrix} -1 & 0 & 1 \\ -2 & 0 & 2 \\ -1 & 0 & 1 \end{bmatrix} \quad (2.10)$$

This metric convolves the image with Sobel operators, and then sums the square of the gradient vector components.

7. Image Power:

$$f(n_z) = \frac{1}{N_x N_y} \sum_{n_x=0}^{N_x-1} \sum_{n_y=0}^{N_y-1} \left[I\left(n_x, n_y, n_z\right) \right]^2 \quad (2.11)$$

This metric squares the grey scale value of each pixel.

8. Variance:

$$f(n_z) = \frac{1}{N_x N_y} \sum_{n_x=0}^{N_x-1} \sum_{n_y=0}^{N_y-1} [I(n_x, n_y, n_z) - mean\{I(n_z)\}]^2 \tag{2.12}$$

Variance measures how far the value of the pixels deviate from the mean. Large values of variance indicate distinct high frequency content in the image. On the contrary, small values of variance indicate homogeneous low spatial frequency image content. The metrics 9 to 11, that follow are slight variations of the variance metric and require no further discussion.

9. Normalized Variance:

$$f(n_z) = \frac{1}{N_x N_y [mean\{I(n_z)\}]^2} \sum_{n_x=0}^{N_x-1} \sum_{n_y=0}^{N_y-1} [I(n_x, n_y, n_z) - mean\{I(n_z)\}]^2 \tag{2.13}$$

10. Absolute Variance:

$$f(n_z) = \frac{1}{N_x N_y} \sum_{n_x=0}^{N_x-1} \sum_{n_y=0}^{N_y-1} |I(n_x, n_y, n_z) - mean\{I(n_z)\}| \tag{2.14}$$

11. Normalized Absolute Variance:

$$f(n_z) = \frac{1}{N_x N_y [mean\{I(n_z)\}]^2} \sum_{n_x=0}^{N_x-1} \sum_{n_y=0}^{N_y-1} |I(n_x, n_y, n_z) - mean\{I(n_z)\}| \tag{2.15}$$

12. Vollath's F4:[50]

$$\begin{aligned} f(n_z) = \frac{1}{N_x N_y} [& \sum_{n_x=0}^{N_x-1} \sum_{n_y=0}^{N_y-1} I(n_x, n_y, n_z) \times I(n_x+1, n_y, n_z) - \\ & \sum_{n_x=0}^{N_x-1} \sum_{n_y=0}^{N_y-1} I(n_x, n_y, n_z) \times I(n_x+2, n_y, n_z)] \end{aligned} \tag{2.16}$$

13. Vollath's F5:[51]

$$f(n_z) = \frac{1}{N_x N_y} \sum_{n_x=0}^{N_x-1} \sum_{n_y=0}^{N_y-1} I(n_x, n_y, n_z) \times I(n_x+1, n_y, n_z) - mean\{I(n_z)\}^2 \quad (2.17)$$

Vollath proposed two focusing metrics with good performance in the presence of noise[50]. F4 is based on the autocorrelation function while F5 is based on the standard deviation function.

14. Contrast:

$$f(n_z) = \frac{max\{I(n_z)\} - min\{I(n_z)\}}{max\{I(n_z)\} + min\{I(n_z)\}} \quad (2.18)$$

where $max\{I(n_z)\}$ and $min\{I(n_z)\}$ are the maximum and minimum values of the entire image. Contrast is a commonly used metric to measure image quality. Mathematically, it equals the difference between maximum and minimum grey-scale values divided by the sum of the maximum and minimum grey-scale values. For an in-focus image containing a high content of image detail the contrast is expected to be relatively large, while for a defocused monotone image it is expected to be relatively small.

15. Histogram Entropy:

$$f(n_z) = -\sum_{i=0}^{255} p_i \times log_2 p_i \quad (2.19)$$

where p_i is the probability of number of pixels' grey-scale value equal to i. It is expected that an in-focus image that has a high content of detail will have an inhomogeneous intensity pattern and will therefore have a broad histogram. In the case of an out-of-focus image which will appear to be more homogeneous a narrower histogram is expected. Considering the limiting cases where (i) all of the pixels have only one constant value, and (ii) all of the pixel values share an equal probability in the image; For the first example, $f(n_z)$ will equal zero since $\log_2 1 = 0$. For the second example $f(n_z) = -256 \times (\frac{1}{256} \times log_2 \frac{1}{256}) = 8$. If investigated image contains highly varying values, its histogram entropy will be greater than for the case where

the image is more homogeneous.

In the following section how these metrics can be applied to image data is demonstrated. By applying any metric above to a sequence of images, whereby the microscope stage is moved in the z direction between captures, the value of $f(n_z)$ can be calculated for n_z=0 $\rightarrow N_z - 1$. In general, for images of opaque absorbing objects, it can be shown that the value of $n_z\Delta_z$ which corresponds to the maximum value of $f(n_z)$ is the most in-focus image. However, for transparent objects this is not the case. As shown below, the value of $n_z\Delta_z$ that corresponds to the minimum value of $f(n_z)$ represents the most in-focus image.

2.2 Comparison of autofocus metrics for unstained transparent cells and absorbing objects

In this section, the 15 metrics introduced in Section 2.1 are applied to stacks of images recorded from (i) an absorbing object and (ii) an unstained transparent cell. In both cases, the autofocus curve, $f(n_z)$ are plotted. In the experiments, various metrics discussed in Section 2.1 are applied to each image in a stack, whereby one focus measurement value is computed for each image in the stack. In all of the results that follow in this chapter, the measured value $f(n_z)$ against the layer numbers n_z is plotted, which corresponds to the position in the stack.

In the case of stained cells or fluorescently labelled cells, previous studies have shown that the position n_z, resulting in the maximum value of $f(n_z)$ corresponds to the correct in-focus plane. For stained cells, the defocused images inherently have less information content than well focused images [52]. Therefore, focus metrics such as those discussed in Section 2.1 respond to the best focal position with a global maximum. In order to demonstrate the behaviour of autofocusing applied to an absorbent object, $N_z = 50$ images of a USAF resolution chart are recorded. Images were recorded using a Nikon Diaphot 300 inverted microscope operating in brightfield mode. The microscope objective that was used in this experiment was a Reichert Plan

Fluor 100×/0.95NA ∞/0. The digital images were captured using a Basler CMOS camera (acA2000-340km) with N_x=2040 and N_y=1088 and pixel sizes of 5.5μm in both the x and y dimension. The path of light through the microscope provides an additional ×2 magnification which results in an effective pixel size of $\Delta_x = \Delta_y$ = 27.5nm. Images were recorded with a sampling interval of $\Delta_z = 1\mu$m. In Fig. 2-1(a), (b) and (c), the recorded image shown for n_z = 22, 25, and 28 respectively corresponding to the image just before, at, and just after the focal plane. In Fig. 2-1(d), $f(n_z)$ is plotted using the variance metric, given in Eqn (12) which is widely used in autofocusing algorithms. It is clear that there exists a clear increase in the value of f as n_z approaches the focal plane followed by a clear decrease as the object moves out of focus. The position n_z, at which the image is most in focus is defined by an obvious maximum in f.

It is usually expected that autofocus algorithms fail to work for transparent objects such as unstained cells. In order to investigate the behaviour of the various focus metrics for a transparent object, the same approach was applied to an unstained cell on a glass slide. In this experiment, a bladder cancer cell (T24) was grown in a cell culture medium and deposited on a glass slide. For this experiment, the same microscope, objective and camera were used but this time the number of images was increased to $N_z = 200$ and the sampling interval was reduced to $\Delta_z = 0.25\mu$m

In Fig. 2-2(a), (b), (c) and (d), the recorded image for four different values of n_z are shown. In Fig. 2-2(a), $n_z = 98$, the image is not in focus and appears blurred. The dark circle around the nucleus and bright circle around the cytoplasm indicate that this image is recorded in an out-of-focus plane. In Fig. 2-2(b), $n_z = 106$, it is clear that the cell cytoplasm has reduced in visibility and the bright circle around cytoplasm has disappeared, suggesting that this part of the cell has come into focus. Dark features that are visible around the nucleus indicate that this part of the cell remains out-of-focus. Moving to Fig. 2-2(c), $n_z = 110$, the nucleus is now in-focus; the dark features around it have disappeared and some detail inside the nucleus appears in this image. Finally in Fig. 2-2(d), $n_z = 115$, the entire cell is once again out-of-focus. Applying the variance metric to this stack of images provides the autofocus

curve shown in Fig. 2-2(e). It is clear that there is an obvious global minimum in the variance curve at the most in-focus position, n_z. This phenomenon results from the image of the cell becoming increasingly homogeneous as it nears the focal plane making it difficult to distinguish the cell from the background and in this case the variance reduces. As described previously, in Fig. 2-2(a) to (d), as the cell moves out of focus, detail in the image develops with corresponding increases in the value of the variance.

In order to compare all of the metrics discussed in Section 2.1, all of them were applied to both the stack of images of the resolution chart and the unstained cyto-spinned T24 bladder cancer cell in and Fig. 2-3(a) and (b) respectively.

As shown in Fig. 2-3(a), all of the metrics provide reasonable performance for the absorbent object, except for metrics (14) and (15). The result of metric (14) is a straight line because the minimum value of the images is always zero in this particular case, leading to the constant contrast$((maxima - 0)/(maxima + 0) = 1)$. Unexpectedly, metric (15) provides a global minimum in this case, where as could have expected a global maximum. This is because the resolution chart image in Fig. 2-1(b) is more homogeneous than Fig. 2-1(a) and (b), which have a greater range of different grey-scale values. Since the histogram entropy decreases when homogeneity increases, It can be seen that for this particular absorbent object this metric provides a global minimum at the correct in-focus plane. This behaviour is dependent on the specific object used in this experiment, whereby the in-focus image essentially contained only two grey scale value. In general, it is expected that this metric will provide a maximum for stained cells.

In Fig. 2-3(b), the same set of results are shown for the stack of images of the unstained T24 cell; It is clear to see that metric (2), (5), (7) are the poorest, since they didn't provide any readable spacial extremum. It can be identified that metrics (1), (3), (4), (6), (12) and (14), all have a local minimum around the correct focal position but are not well pronounced. However, six of the metrics: (8), (9), (10), (11), (13) and (15) all provide smooth and distinctive global minima values corresponding to the most in-focus image. Among those six metrics, four of them, (8), (9), (10) and

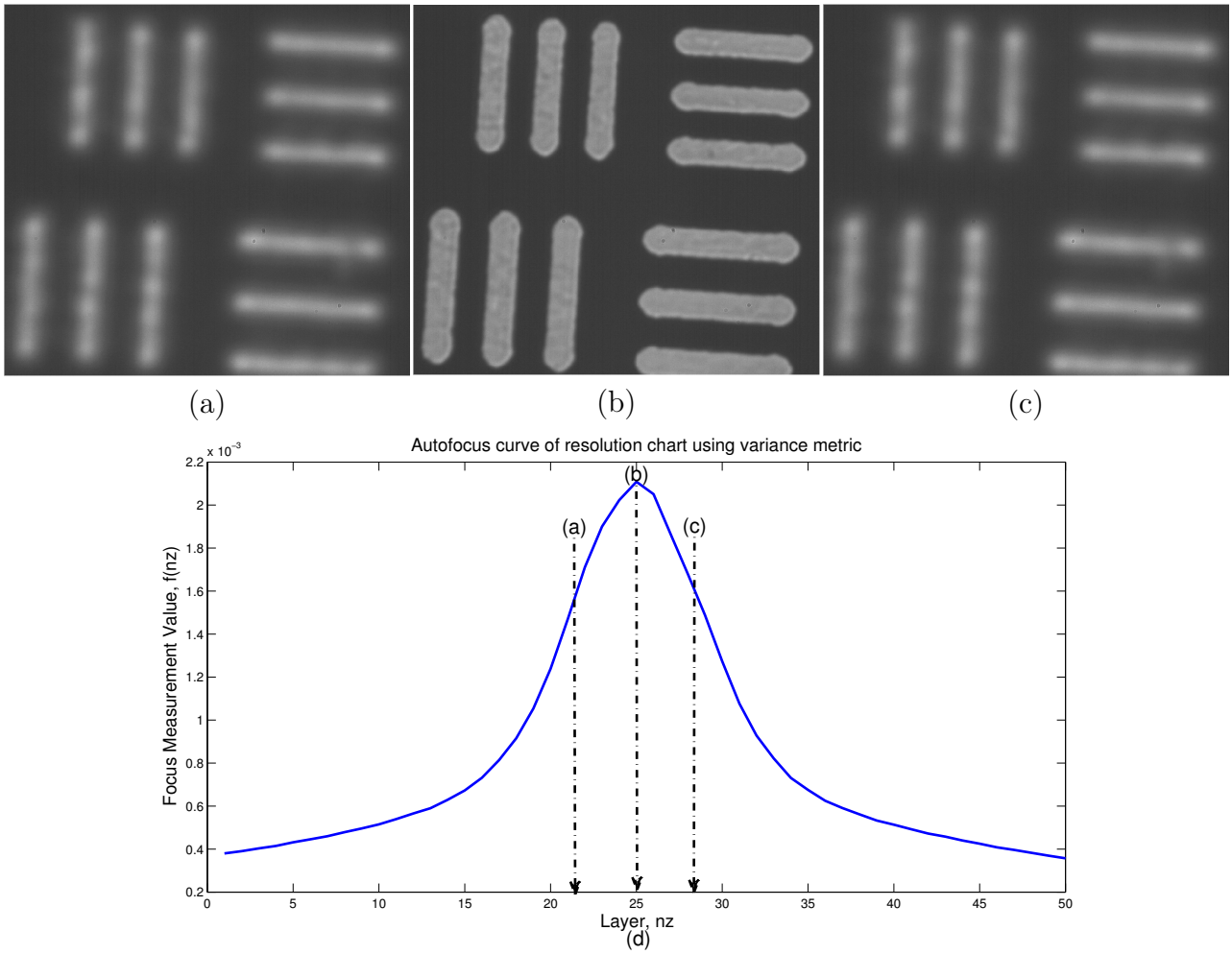

Figure 2-1: Focus steps: (a) under in-focus plane; (b) in-focus plane; (c) above in-focus plane; (d) autofocus curve of resolution chart using variance metric where the position of the planes shown earlier have been indicated using arrows. The sizes of microscope images shown in (a),(b) and (c) are identical which is 20.4μm (width)$\times$18.5μm (height) each.

(11) are all based on variance and they all display similar characteristics. Metric (11) is selected from this group of four for further study as its curve shows the greatest difference between maximum and minimum focus measurement values.

Comparing Fig. 2-3(a) and (b), the most significant difference is that transparent cells return a minimum rather than the maximum for the case of the absorbent object. In the next section, three of the best behaving metrics were selected for further evaluations namely; (11) normalized absolute variance, (13) Vollath's F5 and (15)histogram entropy for further evaluation.

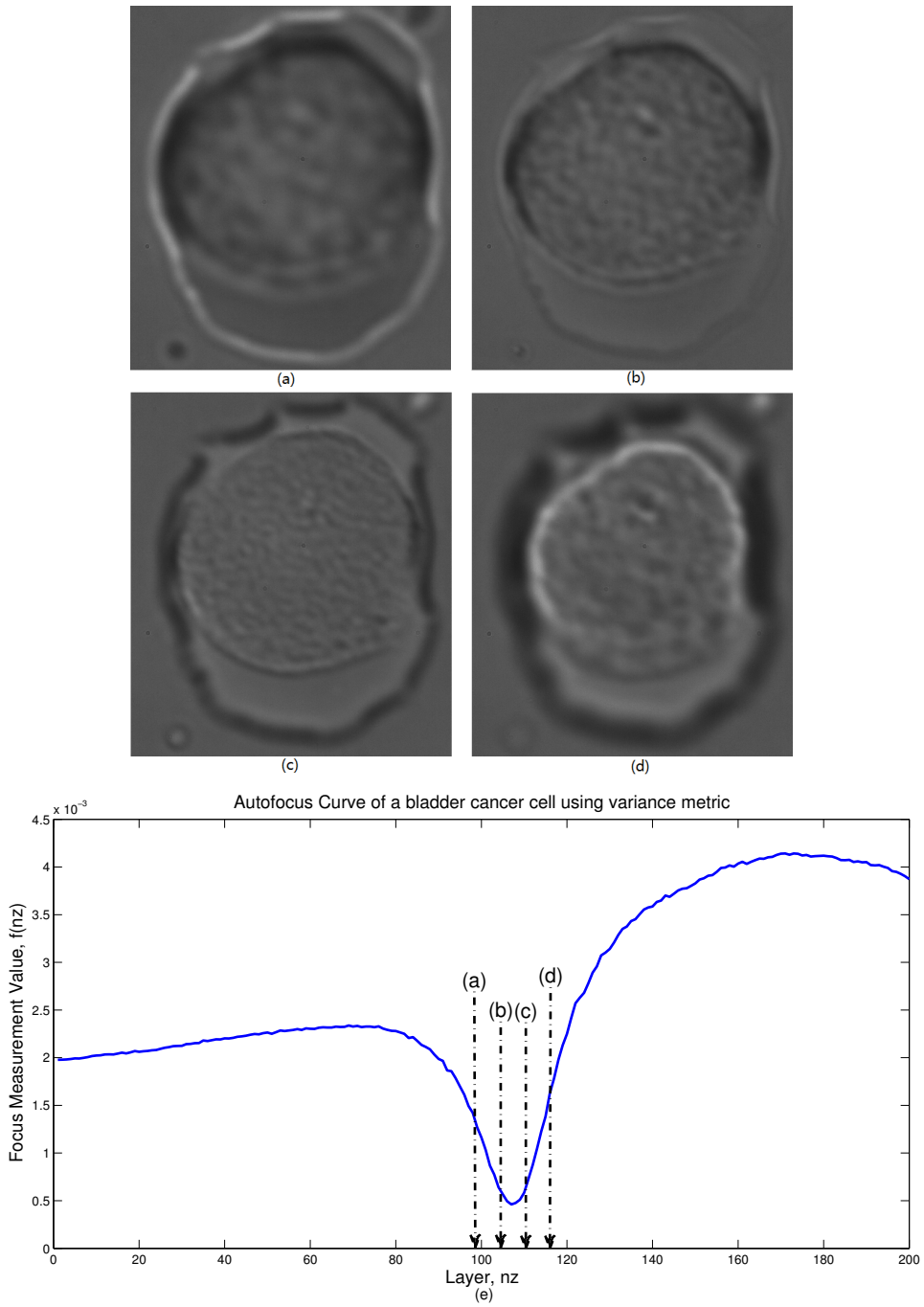

Figure 2-2: Focus steps: (a) under in-focus plane; (b) cytoplasm in-focus; (c) nucleus in-focus; (d) above in-focus plane; (e) Autofocus curve of the bladder cancer cell using the variance metric where the focus planes that are shown in this figure are clearly indicated using arrows. The sizes of microscope images shown in (a),(b),(c) and (d) are identical which is 12.57μm (width)$\times$14.3μm (height) each.

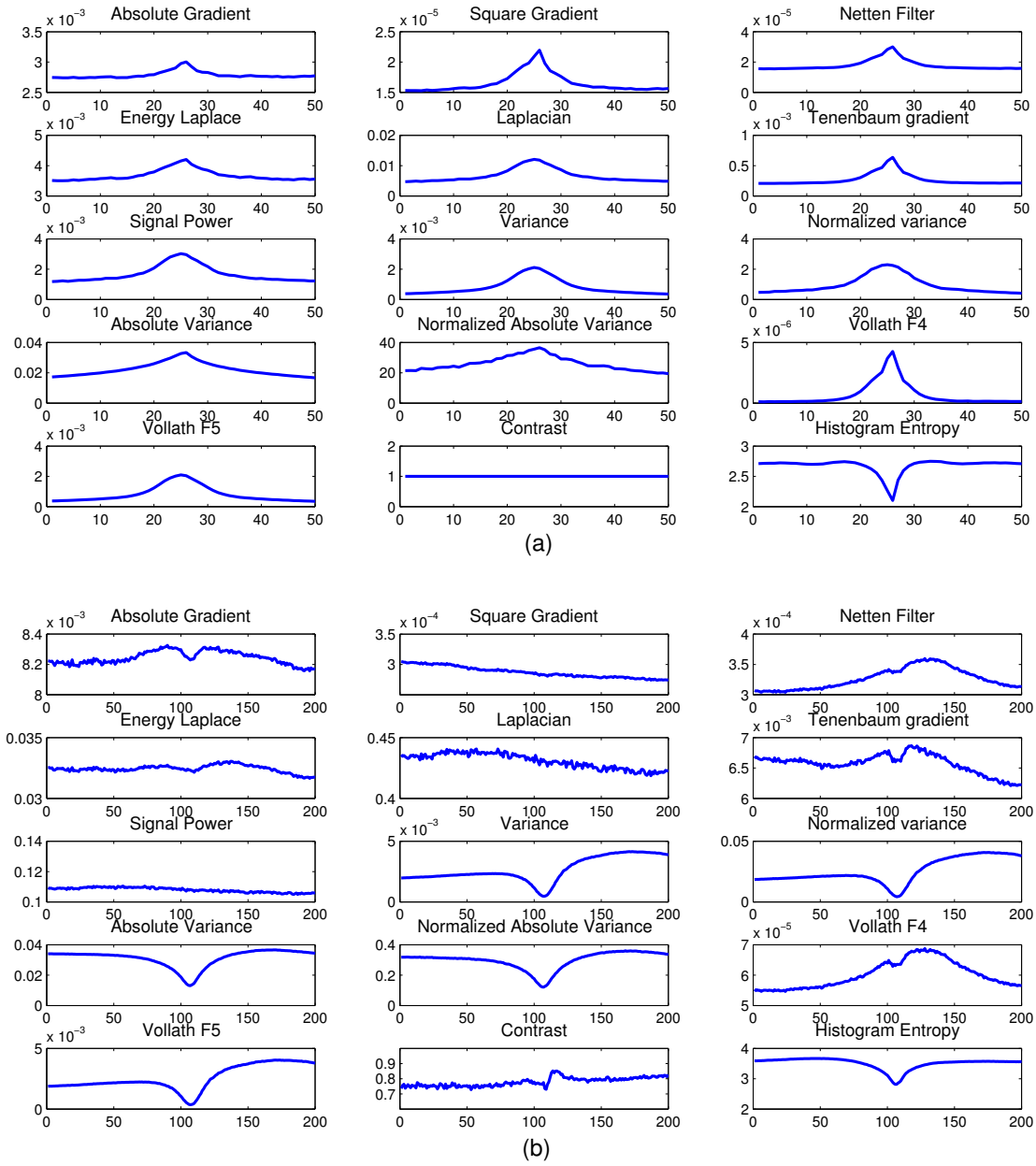

Figure 2-3: Result of the metrics in Section 2.1 applied to (a) the stack of 50 images of the USAF resolution chart; (b) the stack of 200 images of the unstained T24 bladder cancer cell.

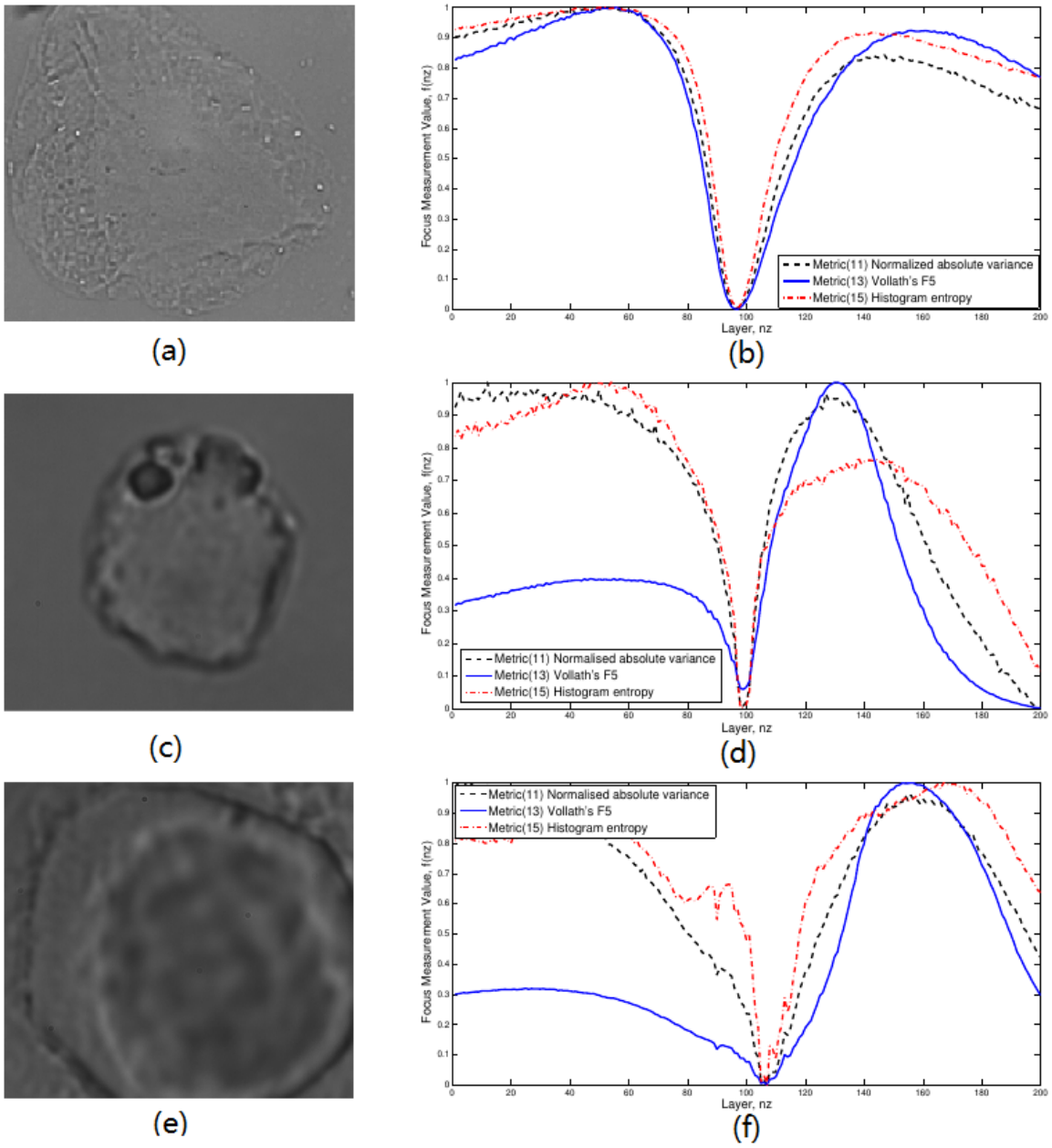

Figure 2-4: (a):In-focus images of cheek cell, $n_z = 97$, size is 35.26μm (width)$\times$28.66μm (height); (b): Comparison of the three selected metrics applied to the cheek cell; (c): In-focus images of Blast cell, $n_z = 99$, size is 17.66μm (width)$\times$14.38μm (height); (d): Comparison of the three selected metrics applied to the Blast cell; (e): In-focus images of bladder cancer cell, $n_z = 107$, size is 17.66μm (width)$\times$14.38μm (height); (f): Comparison of the three selected metrics applied to the Bladder cancer cell.

2.3 Evaluation

To confirm the repeatable performance of the results shown in Section 2.2, three of the best behaving metrics were proceeded to be selected and apply them on different unstained cells. All the images were recorded using the same Nikon Diaphot 300 microscope used in the previous experiment, once again operating in brightfield mode. The experimental parameters for the three cells are shown below in Table. 1, and all the focus curves shown in Fig. 2-3 are normalized by first subtracting the minimum value followed by dividing by the maximum value of the result in order to visualize all three metrics on the same scale.

Cell	Magnification	NA	N_x	N_y	N_z	Δ_x	Δ_y	Δ_z
Cheek	50	0.8	2040	1088	200	55nm	55nm	0.1μm
Blast	100	0.95	2040	1088	200	27.5nm	27.5nm	0.25μm
T24	100	0.95	2040	1088	200	27.5nm	27.5nm	0.25μm

Table 2.1: Experimental parameters for three unstained cells

From Fig. 2-4, it is clear to see that all three metrics repeatedly provide very obvious and reliable minima for all three cells. This result is similar to any other cells that were tested, which are not described in this chapter. Normalized absolute variance, Vollath's F5, and histogram entropy are proven to provide robust performance for autofocusing where a minimum indicates the most in-focus distance, as opposed to the more traditional case of finding a maximum value for opaque absorbent objects. In order to compare the computational speed of all three metrics, they were tested using an Intel Core i7 2.4GHz processor by implementing them in MATLAB R2013b. For the images sizes indicated in Table 1, Vollath's F5 required twice as much processing time as the other two metrics. Histogram Entropy is slightly faster than Normalized absolute variance.

2.4 Conclusion

In this chapter the first comprehensive investigation on the application of autofocusing metrics to images of unstained transparent cells obtained using brightfield microscopy was provided. In Section 2.1 15 autofocus metrics were reviewed and in Sections 2.1 and 2.2 all of them were applied to stacks of images obtained from (i) an opaque absorbent object in the form of a USAF resolution chart and (ii) an unstained bladder epethelial cell. It was found that instead of obtaining a local maximum at the correct focal distance for the case of an absorbent object, a local minimum is found for unstained transparent cell indicating the correct in-focus plan. After comparing the performance of all 15 metrics, three were selected for further study: normalized absolute variance, Vollath's F5 and Histogram Entropy. These three metrics appear to provide reliable autofocusing are for unstained cell images recorded by brightfield microscope since they have smooth focus curves with a very obvious global minimum at the correct distance. This conclusion was confirmed in Section 2.3 by applying the three metrics to three different cells: a cheek cell, a blast cell and a second bladder cancer cell respectively. Finally, took computation time into consideration: normalized absolute variance and histogram entropy require approximately half the time of Vollath's F5. The work presented in this chapter has been published in a recent conference proceeding[44].

Chapter 3

Recovering the three dimensional morphology of unstained cells using brightfield microscopy

In the previous chapter, the phenomenon that unstained cells are often effectively transparent and appear to have an homogeneous intensity profile when they are in focus has been addressed. In this chapter, a method is proposed to recover information about the morphology of an unstained cell using brightfield microscopy and the autofocus algorithm introduced in chapter 2, which is based on recording a stack of images where the sample is mechanically moved by sub-micron amounts between captures. The implementations of proposing algorithm is provided using both central processing unit(CPU) and graphic processing unit(GPU). The experimental results demonstrate the usefulness of the method. This approach is expected to have application in various forms of clinical cytology and as a useful adjunct in the automation of Raman and FTIR micro-spectroscopy systems.

The idea of applying autofocusing to regions across a stack of microscopic images is not new. In Ref. [53], B. Forster et. al. concluded that there are three different approaches for the purpose of extracting information on the three dimensional shape of the object under investigation: (i) Pixel-based methods[54] compare pixels with same coordinates across each image in the stack and the most in-focus plane for a

given pixel is determined by applying a maximum selection rule on the grayscale value of pixels; (ii) Region-based methods[55] apply a metric to a block of pixels across each image in the stack. The most in-focus plane for that region is determined according to a given selection rule and that depth is assigned to the pixel at the centre of that region; (iii) Multiresolution-based methods[56] are based on the assumption that in-focus regions contain more high frequency components. Among the multiresolution methods, the wavelet transform offers good performance[53]. All of the methods proposed to date for the recovery of three dimensional images from stacks of two dimensional microscopic images have been based on the principle that areas that are in focus contain more detail than areas that are out of focus. However, in the case of unstained transparent cells, this is not true and all of these algorithms fail[53]. In this chapter, an adaptation of the region based method is investigated such that three dimensional images can be recovered from phase only objects. This algorithm is based on recent work where the application of autofocus algorithms to unstained cells was investigated[44].

In Chapter 2, (and also in a recent publichation [44]) the application of auto-focusing algorithms are investigated to images of unstained cells using brightfield microscopy. Although autofocusing has a long history in microscopy,[42][43] previous investigations focused on objects that absorb light; after recording a stack of images where between captures the object is moved relative to the microscope objective, a metric is then applied to each image in the stack and the image that results in this metric having a maximum value is taken to be the most in-focus image. These metrics universally work based on the idea that when the image is in focus, more image detail can be observed and so they often quantify the amount of high frequency content or variance in the image. However, for the class of objects that appear to have an homogeneous intensity pattern such as transparent cells, it is well known that these metrics fail. In the previous chapter and the corresponding paper[44], the application of fifteen well known autofocusing metrics to unstained cells were investigated and the behaviour of these metrics were compared with that of an opaque object, also recorded using brightfield microscopy. How these metrics can be adapted to work

for transparent cells were demonstrated and which metrics provide the best results were determined. In this chapter follow-on investigations are conducted in order to show that these metrics can be applied in a similar manner to sub-regions within the image, thereby providing a spatial resolution on the focal depth of the unstained cell which in turn enables us to extract information on the three dimensional cellular morphology.

In Raman micro-spectroscopy, it is often preferable to select a point within the nucleus when recording the spectrum of a cell for the purpose of diagnostics or for comparing biochemistry across different cells. Staining of cell nucleus is not an option in this case as the additional chemicals corrupt the recorded spectrum and may give rise to either fluorescence or photo-damage. Without staining is difficult to estimate the depth and position of the nucleus using brightfield microscopy. The failure to align the nucleus with the source laser can lead to reduced sensitivity for Raman diagnostics[12]. The method proposed in this chapter can be used as a useful tool for the optimal alignment of cells for Raman microspectrosocpy. Furthermore, it may be possible to employ this algorithm as part of an automated process for preforming Raman based cytology for high throughput diagnostics[12][14].

3.1 Autofocus of sub-regions for unstained cells

The core part of this proposing algorithm is the application of an autofocusing metric to images of unstained cells introduced in Chapter 2. In the previous chapter, fifteen commonly used autofocus metrics were investigated for images of unstained cells and three optimal autofocus metrics were identified: normalized absolute variance, Vollath's F5 and histogram entropy. The mathematical expressions of these three metrics are shown below:

1. Normalized Absolute Variance:

$$f(n_z) = \frac{1}{N_x N_y [mean\{I(n_z\Delta z)\}]^2} \sum_{n_x=0}^{N_x-1} \sum_{n_y=0}^{N_y-1} |I(n_x\Delta x, n_y\Delta y, n_z\Delta z) - mean\{I(n_z\Delta z)\}| \tag{3.1}$$

where I represents the image recorded by a digital camera; n_x and n_y take the range of 0 to $N_x - 1$ and 0 to $N_y - 1$ where N_x and N_y are the number of pixels in the x and y directions respectively; Δx and Δy represent the camera pixel size in the x and y directions respectively and Δz is the distance the stage is moved between the capture of subsequent images in the vertical direction; n_z takes the range of 0 to $N_z - 1$ where N_z is the total number of images recorded.

Large values of variance indicate distinct high frequency content in the image. Conversely, small values of variance indicate homogeneous low frequency image content. In Ref. [44] it was demonstrated that for images of high contrast opaque objects the variance has a maximum value when the image is in focus, while for homogeneous phase only objects the variance has a minimum value.

2. Vollath's F5:[51]

$$f(n_z\Delta z) = \frac{1}{N_x N_y} \sum_{n_x=0}^{N_x-1} \sum_{n_y=0}^{N_y-1} \Big\{ I(n_x\Delta x, n_y\Delta y, n_z\Delta z) \times I(n_x\Delta x + 1, n_y\Delta y, n_z\Delta z) - mean\{I(n_z\Delta z)\}^2 \Big\} \tag{3.2}$$

This metric is based on the standard deviation function which compares the difference between the product of a pixel and the grayscale value of its neigboring pixels with the square of the mean grayscale value. It has been demonstrated to provide good performance in the presence of noise[50][51].

3. Histogram Entropy:

$$f(n_z\Delta z) = -\sum_{i=0}^{255} p_i \times log_2 p_i \tag{3.3}$$

where p_i is the probability of a pixels' grayscale value equal to i. It is expected that an image that has high detail content will have an inhomogeneous intensity pattern and will therefore have a relatively broad histogram. In the case of an image that is more homogeneous, a narrower histogram is expected.

In Chapter 2, these metrics were applied to each image in a stack of images, where the object was moved in the vertical direction between captures. In this section, a similar analysis are applied, but this time the investigation is focused on sub regions within the images in the stack. In order to determine which metric provides the best performance, all three metrics are applied to a number of different regions located in different areas within the image of the cell. The size of the region is an important parameter in this investigation and so the analysis was repeated for a range of different block sizes in order to establish the best performing block size. The result is shown in Fig. 3-1, where in regions that are representative of different focal depths are marked with different colours and the same colours are used in the corresponding focus curves.

The sample used in this experiment is an unstained bladder cancer cell with 200 images in total. Images were recorded using a Nikon Diaphot 300 inverted microscope operating in brightfield mode. The microscope objective that was used in this experiment was a Reichert Plan Fluor $100\times/0.95$NA $\infty/0$. The digital images were captured using a Basler CMOS camera (acA2000-340km) with N_x=2040 and N_y=1088 and pixel sizes of 5.5μm in both the x and y dimension. The path of light through the microscope provides an additional $\times 2$ magnification which results in an effective pixel size of $\Delta x = \Delta y = 27.5$nm and the translation stage was moved in the vertical direction between captures with a sampling interval of $\Delta z = 0.25\mu$m. The highlighted grey area on the curves represent the full depth of field that is selected for further analysis, which corresponds to the images in the stack given by n_z= 92 $\rightarrow$ 122. This range is selected based on the global in-focus image, which is determined to be at n_z= 107, and the range of interest that estimated using a priori knowledge of the approximate cell height. The first column in Fig. 3-1 displays the focus curves generated for all three metrics using a block size of 10 by 10 pixels. The normalized absolute variance and Vollath's F5 have clearly identifiable local minima (red and yellow) at the correct focal planes but regions inside the nucleus (green, blue and black) return no significant features on the curves. The histogram entropy performs poorly for all of the regions but the general performance improves when a 30 by 30 block size is used as shown in the second column in Fig. 3-1. However, it remains

difficult to identify discernible minima for regions inside the nucleus. However, when the block size is increased to 50 by 50 pixels, the minima are clearly identifiable for all cases, indicating the correct focal planes. Thus, a trade-off exists between the accuracy of results in the z directions and the spatial resolution of the depth map in the horizontal plane. Repeated experiments have shown that a 50 by 50 pixel block size is the best compromise for the testing system in order to guarantee reasonable performance. However, it has been found that the block size should be varied on a case by case basis, as factors such as magnification, numerical aperture, camera pizel size and cell type can impact on the performance for a given block size. The normalized absolute variance was selected for further investigation, as it appear to be the most accurate of the three metrics in general.

In order to automatically identify the correct local minimum on the focus curve within the range of interest, the Savitzky-Golay filter[57] is used to smooth the data. The difference between the original curve and the Savitzky-Golay filtered curve highlights the sharp changes in the original focus curve; in this way the correct focal plane is indicated by a global minimum instead of a local minimum which facilitates simpler automatic identification. In Fig. 3-2, the application of the Savistky-Golay filter is illustrated to focus curves corresponding to two regions within the cell; the data shown in red corresponds to a relatively higher region in the cell nucleus and the data in blue corresponds to a lower region in the cytoplasm. In Fig. 3-2 (b) and 3-2 (c), it is shown that the original focus curve using normalised absolute variance and the filtered version of the same curve corresponding to the higher region in the cell. It is clear that, within the region of interest, the original focus curve does not return a global minimum at the correct plane, but this is found to be the case for the filtered data. However, for lower regions it is found that, specifically within the cytoplasm, which contains very little image detail when in-focus, the global minimum of the Savitsky Golay filtered data does not correspond to the correct focal plane; rather in this case, the global minimum of the original autofocus curve is more reliable. This is illustrated in Fig. 3-2 (d) and Fig. 3-2 (e). In general, it has been found that combining both approaches returns the most accurate depth map for the entire

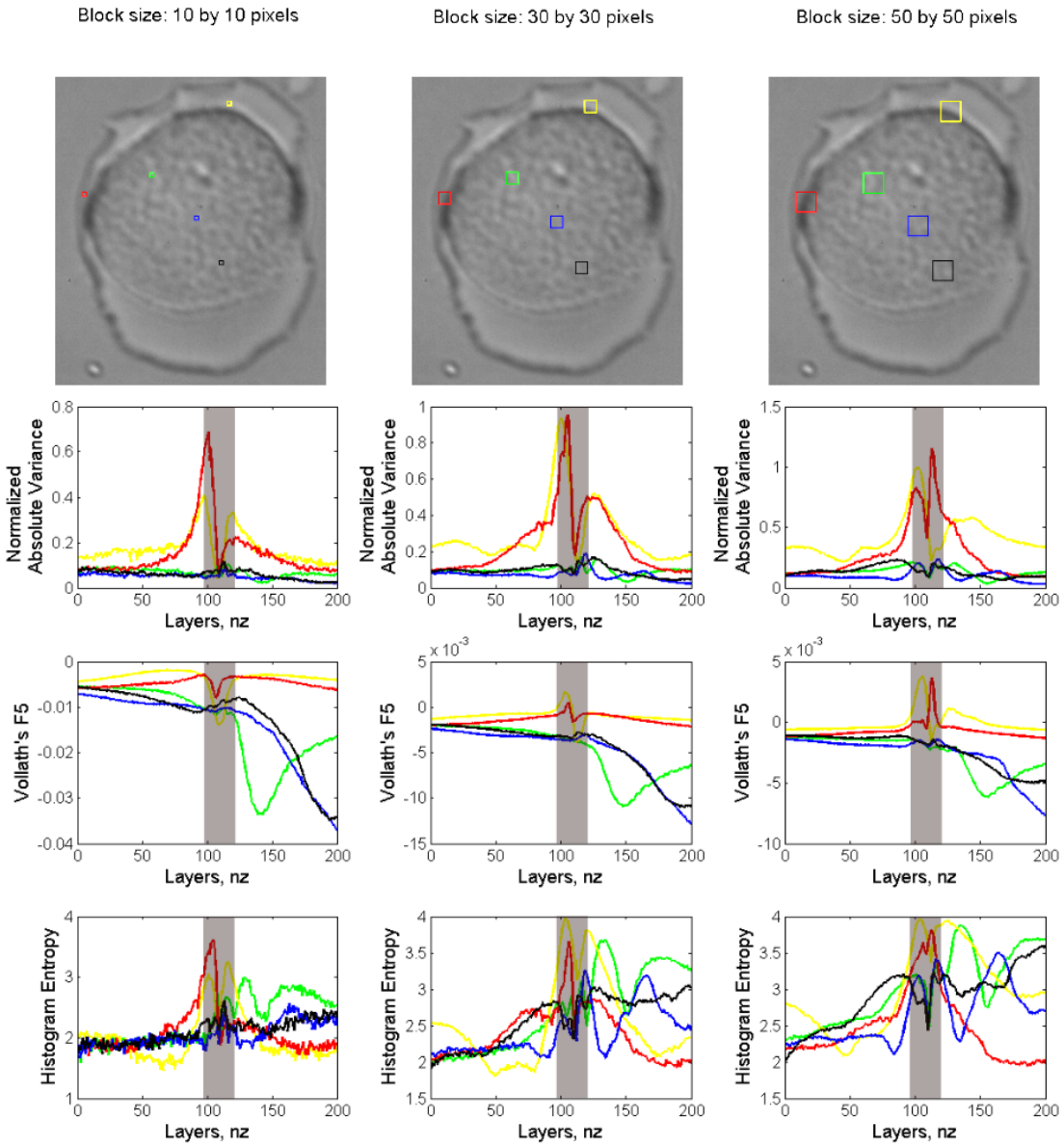

Figure 3-1: Comparison of performance of three autofocus metrics: Normalized absolute variance, Vollath's F5 and histogram entropy with three different block sizes: 10 by 10, 30 by 30, 50 by 50 pixels. The sizes of microscope images shown in the first row are identical which is 12.57μm (width)$\times$14.3μm (height).

cell. For a given region, the location of the global minimum of the autofocus curve within the region of interest is taken to correspond to the correct focal plane, except when that location is higher than the global in-focus plane of the overall image; for these higher regions the location of global minimum of the filtered curve is used.

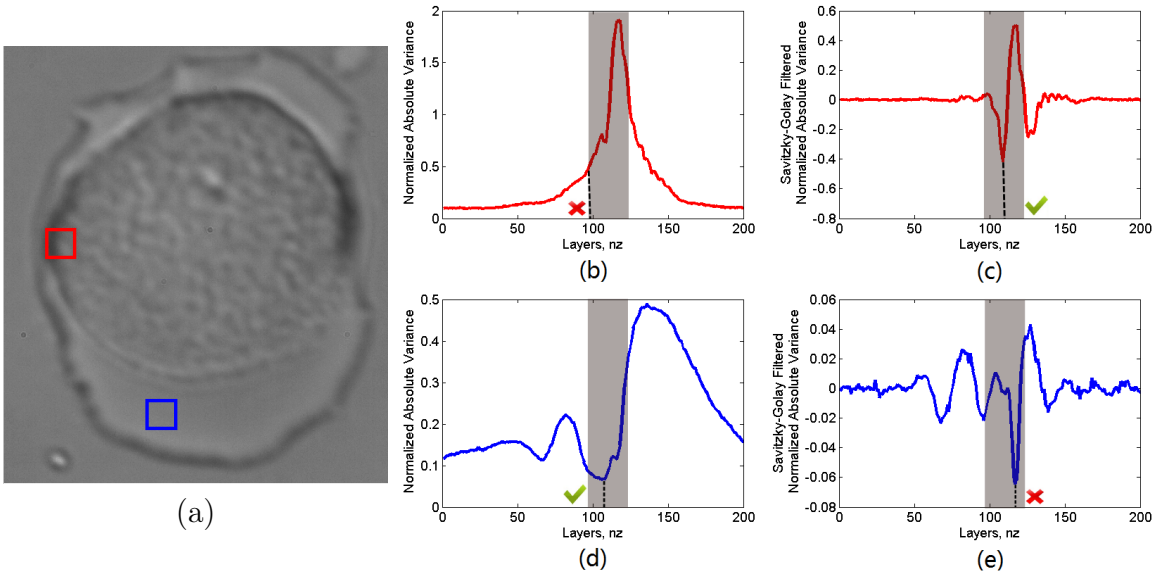

Figure 3-2: Examples of failed regions using normalised absolute variance global minimum and Savitzky-Golay filtered global minimum (a) two example problem regions of a bladder cancer cell, image size is 12.57μm (width)×14.3μm (height); (b) normalized absolute variance curve of red region; (c) Savitzky-Golay filtered normalized absolute variance curve of red region; (d) normalized absolute variance curve of blue region; (e) Savitzky-Golay filtered normalized absolute variance curve of blue region.

3.2 Algorithm for recovering 3D cell morphology

3.2.1 Methodology

In this section, a basic algorithm is proposed for the recovery of a continuous 3D morphology of an unstained cell using the principles developed in Section 3.1. Two different approaches are considered; the relatively simpler case where the regions are non-overlapping and the more computationally intensive case where overlapping blocks were considered. In the non-overlapping case, illustrated in Fig. 3-3 (a), each image in the stack is divided into many small non-overlapping blocks with uniform

size. The previously described autofocus metric is applied to each block throughout the stack, revealing the correct focus depth for each particular region. The focal depth for a given block is assigned to the centre pixel in that block and the resulting depth map has a low spatial resolution, with N_x/B_x and N_x/B_x samples with sampling intervals of $\Delta x B_x$ and $\Delta y B_y$ in the x and y directions respectively, where B_x and B_y denote the block size in pixel numbers. For the overlapping case, the block window moves pixel by pixel and the focus depth that is computed for a given block is assigned to the middle pixel in the block, as illustrated in Fig. 3-3(b). At the end of this process, a new image with the same size of the original image is generated in which the value of each every pixel in the new image corresponds to the focal depth of the corresponding block. Clearly the non-overlapping case provides a low resolution depth map but it has the advantage of being relatively light in terms of computation. The overlapping case on the other hand can provides a high-resolution depth map has a heavy computational load.

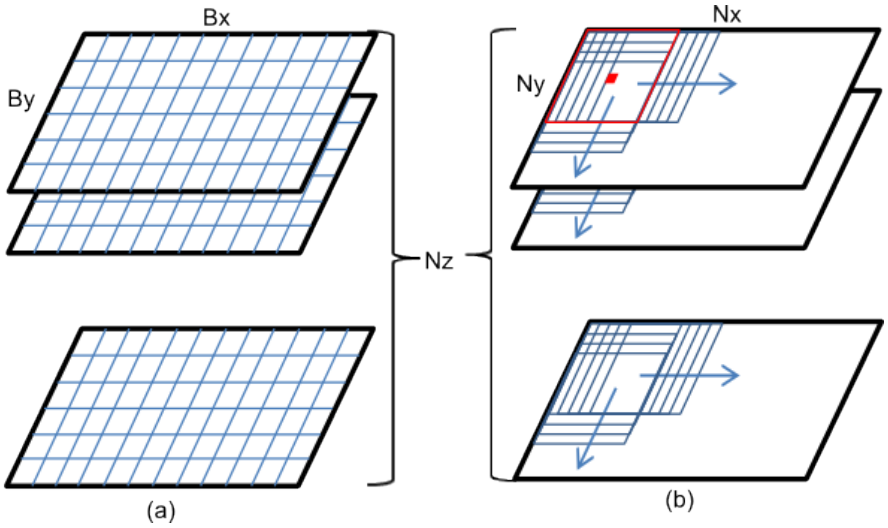

Figure 3-3: (a) non-overlapping and (b) overlapping methods to apply autofocusing algorithms

Regardless of which if these two methods is used to generate the depth map, the same autofocus metric is applied to each block, as discussed in Section 3.1. Following calculation of the raw depth map, thresholding is necessary in order to identify those pixels which correspond to background and contain no meaningful object data. The

focus curve relating to background pixels is highly random and has a low amplitude relative to data from object pixels. For this reason, basic thresholding can be applied to identify background pixels and a constant depth value is assigned to these pixels equal to the minimum value that is calculated from the object pixels. A trade-off where high threshold values result in a cleaner background but have the drawback of incorrectly assigning some object pixels as background, thereby creating holes or gaps within the object depth map. Thus, a tunable threshold is built into the GUI that was designed for this application. When selecting the choice of threshold, small holes are tolerable in order to ensure a clean background. The final step in proposing algorithm is to fill small holes.

3.2.2 Fast algorithm

As previously discussed in section 3.2.1, the overlapping method is very timeconsuming. For an image of size $(N_x,N_y) = (1088,2040)$ and a block size of $(B_x,B_y) = (50,50)$, the non-overlapping method results in approximately 840 separate block calculations while the overlapping case results in over two million. Comparing the speed of applying normalized absolute variance and the histogram entropy metric on a single 50 by 50 block in MATLAB 2013b, normalized absolute variance takes 2.2s to generate the focus curve, which is faster than 2.7s using the histogram entropy metric. The most significant part of this process involves opening and closing each image in the stack, which is necessary due to the large amount of data involved compared with available RAM. Applying the normalised variance metric to all blocks in the overlapping case for the image size and block size metioned above requires a stack of approximately 70 seconds with MATLAB. Applying the same approach to the non-overlapping case results in a time of approximately 100 days of computation time. However, it is possible to implement the overlapping method in a significantly shorter time by employing the Fast Fourier Transform (FFT) algorithm as described below.

Taking another look at Equation (3.1), a core element in the calculation of the autofocus metric is to numerically calculate the mean value of a given block. For the overlapping case, this process needs to be repeated for every overlapping block

of B_x by B_x pixels. This process is recognised as equivalence as convolving the image with a rectangular function of width B_x and B_y in the x and y directions and height $1/(B_xB_y)$. The value of each sample in the resulting 2D image represents the mean value for a block centred at that sample location. Such a convolution can be implemented using the FFT algorithm; convolution with a rectangular function in the space domain is equivalent to multiplication with a sinc function in the spatial frequency domain[58]. The process of calculating the mean values of each block can be described as follow as follows

$$M\left(n_x\Delta x, n_y\Delta y\right) = \mathcal{F}^{-1}\left\{B_xB_ySinc\left(B_xm_x\Delta f_x, B_ym_y\Delta f_y\right) \times \mathcal{F}\left\{I\left(n_x\Delta x, n_y\Delta y\right)\right\}\right\} \tag{3.4}$$

where $\mathcal{F}\{\cdot\}$ and $\mathcal{F}^{-1}\{\cdot\}$ denote the operators for the Discrete Fourier Transform and Inverse Discrete Fourier Transform respectively, both of which can be implemented using the FFT algorithm; $\Delta f_x = 1/(N_x\Delta x)$ and $\Delta f_y = 1/(N_y\Delta y)$ and M denotes the matrix containing the mean values of each block. Appropriate zeropadding is required before the first DFT, see [58]. The multiplication step in the equation above denotes element-by-element multiplication and not matrix multiplication, i.e. $a(1,1) = b(1,1) \times c(1,1)$.

The overall process of obtaining the depth map can be calculated according to the following equation:

$$D(n_x, n_y, n_z) = \frac{\left|I\left(n_x, n_y, n_z\right) - M\left(n_x, n_y, n_z\right)\right|}{N_xN_yM\left(n_x, n_y, n_z\right) \times M\left(n_x, n_y, n_z\right)} \tag{3.5}$$

Again, the multiplication and division in the above equation are element-by-element and not matrix operations. The above equation is calculated for each value of n_z in the stack, providing the raw data that is then analysed as described in Section 3.1. Simple averaging is requires B_xB_y additions and for the overlapping methods this averaging needs to be repeated $N_xN_yN_z$ times which results in $B_xB_yN_xN_yN_z$ numerical operations. Using the FFT approach this reduces to approximately $2N_zN_xN_y(\log_2 N_x + \log_2 N_y)$, assuming a radix 2 FFT. This accounts for approximately a 60 times speed

up over the direct approach.

3.2.3 GPU implementation

Although fast algorithm is implemented to speed up the computation time, the total calculation is still need more than an hour to get result from MATLAB using a continuous way. Thus, the proposing 3D morphology recovery algorithm is implemented using GPU.

The forward and inverse FFTs for the fast evaluation of the convolution operations for the mean and variance calculations of the normalized absolute variance autofocus metric are carried out using GPU computation. CUDA[59] programming language is used for the GPU implementation and highly optimized CuFFT library[60] is used for the FFTs. Since the input and output data are real valued for these convolutions, real to complex 2D FFTs for the forward case and complex to real 2D FFTs for the inverse case are used to reduce the computation amount by half using the mirror symmetry observed in these types of FFT operations. The mean kernel multiplication between the forward and inverse FFTs is also carried out on the GPU device avoiding the transfer of the intermediate data between the host computer and the GPU device. The complete GPU computation of the autofocus metric includes the following steps for each separate image of the stack: 1) Initial image pixel values are transferred to the GPU memory and zero padded to make the dimensions suitable for GPU computation. 2) Convolution for the mean calculation is carried out using forward and inverse FFTs and intermediate kernel multiplication is applied as described above. 3) Convolution for the variance calculation is carried out by the repetition of the previous step. The input for this second convolution is calculated as the mean image pixel values subtracted from the original image pixel values (absolute value is taken after the subtraction). 4) Calculated variance image pixel values are divided by the square of the mean image pixel values.

The autofocus metric is calculated for the stack of images on the GPU. The resultant autofocus metric images are gathered together as a 3-dim stack and transposed to establish data locality in the z-axis which holds the data for the focus curves

(autofocus metric values of separate images for a specific pixel). The transposed 3 dimensional stack data is transferred to the host computer for Savitzky-Golay filter application on the CPU. The local minima identification is carried out on the GPU for each pixel after the Savitzky-Golay filtered curves are subtracted from the original focus curves and transferred back to GPU memory. Each GPU thread is responsible for a separate focus curve in the local minima identification GPU kernel and thus a high degree of parallelization is established. The depth map image is constructed from the local minima values for each pixel and a median filter is applied to smoothen. This resulted depth map image is transferred back to host computer.

3.3 Experimental Results

All the images were recorded using the same Nikon Diaphot 300 microscope and digital camera described in Section 3.1, once again operating in brightfield mode. The other variable parameters are listed in table 3.1. Two cells were investigated; the first was a fresh cheek cell smeared onto a glass slide and the second was a bladder cancer cell cultured, and dropped onto a glass slide.

Cell	Magnification	NA	Pixel size Δx	Pixel size Δy	Step size Δz	n_z
Cheek	50	0.8	0.055μm	0.055μm	0.1μm	200
Blast	100	0.95	0.0275μm	0.0275μm	0.25μm	200

Table 3.1: Experimental parameters for two unstained cells

Fig. 3-4 shows the result of applying the algorithm described in previous sections to a normal cheek cell using both the non-overlapping and the overlapping methods. In this experiment, normalized absolute variance is used and a block size given by $(B_x,B_y) = (50,50)$. In Fig. 3-4(a) and (b) the depth maps recovered from both methods is shown. It can be seen that they both provide a similar morphology but with different spatial resolutions; (a) can be considered as a down sampled version of (b). Fig. 3-4(c) is the most in-focus image in the stack without any processing and Fig. 3-4 (d) is extended depth-of-focus image that is generated by using the

most in focus values for each pixel value throughout the stack, according to the depth map. Interestingly, there is even reduced image detail visible in the extended focus image, further highlighting the point that a transparent cell is a phase only object and detail can only be observed indirectly by analysing an out-of-focus image. Fig. 3-4(e) illustrates a contour map that overlies the original unprocessed cell image and highlights regions of similar depth. It is interesting to note that the cell can be segmented accurately using this contour map. Finally, in (f), the original image with the highest area marked in green is shown, presumably the cell nucleus. This image is similar to staining and it is of particular interest in the context of those applications where identification of the cell nucleus is important and where it is preferable not to perform chemical staining.

Fig. 3-5 shows the result of applying 3D morphology recovery algorithm on a bladder cancer cell in both non-overlapping and overlapping case. In this case, the block size is increased to 60 by 60 pixels to show that 50 by 50 pixels is the recommended minimum block size but slightly increasing the size is acceptable and will lead to smoother morphology. Fig. 3-5 (a) and (b) are the non-overlapping and overlapping 3D plot respectively and again, they are very similar and (a) is the down-sampled version of (b). Fig. 3-5 (c) is the original most in-focus image without any image processing. It is clear to see that the enlarged dark nucleus in the center of the cell which is clearly not in focus. Fig. 3-5 (d) is the extend depth of focus image of this cell where everything are in focus including the partial cell in the upper left corner. Fig. 3-5 (e) and (f) are the contour and highlighted nucleus on top of global in-focus image obtained by applying different thresholding on the non-overlapping depth map. Basiclly, with the depth map, any part of the cell can be identified and segmented like nucleus and cytoplasm very easily.

3.4 Conclusion

In this chapter, a 3D morphology recovery algorithm was introduced for unstained cells recorded using brightfield microscopy that is based on the results in Chapter

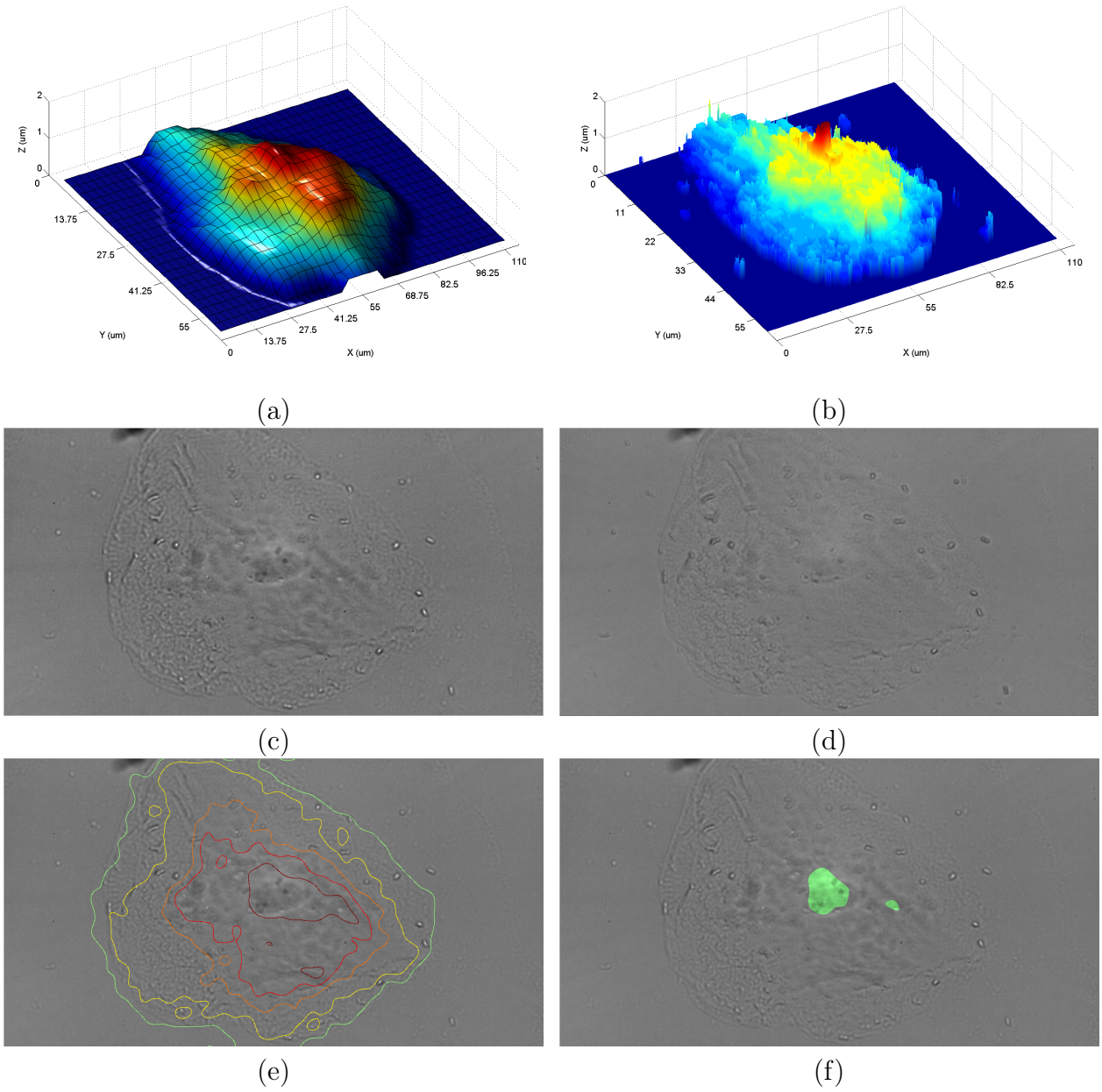

Figure 3-4: Normal cheek cell (a) non-overlapping 3D morphology plot; (b) overlapping 3D morphology plot; (c) global in-focus image; (d) extended depth of focus image; (e) contour map; (f) highlighted nucleus image. The size of microscope images shown in (d),(d),(e) and (f) are identical which is 112.2μm (width)$\times$59.84μm (height).

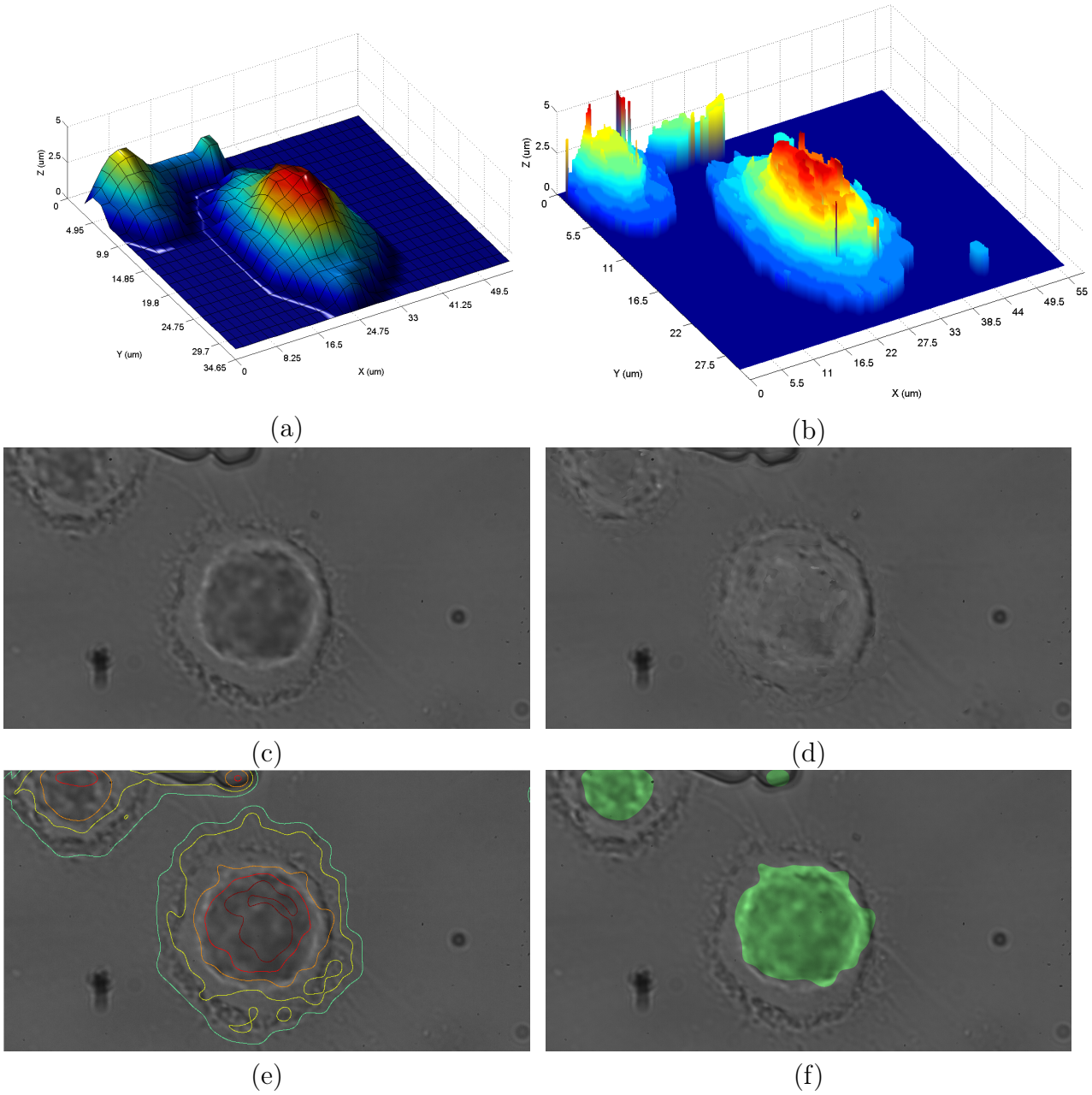

Figure 3-5: T24 bladder cancer cell (a)non-overlapping 3D morphology plot; (b)overlapping 3D morphology plot; (c)global in-focus image; (d)extended depth of focus image; (e)contour map; (f)highlighted nucleus image. The size of microscope images shown in (d),(d),(e) and (f) are identical which is 56.1μm (width)$\times$29.92μm (height).

2, where the application of autofocus metrics to images of unstained cells was investigated. Making use of the special property that unstained cells become effectively transparent when they are in-focus an autofocus algorithm for unstained cells was developed. In this chapter, the application of the metrics discovered in Chapter 2 to sub-regions with cell image was investigated in order to identify the focal depth of small areas in the image. In this way, a depth map can be created that reveals information about the three dimensional cellular morphology. Two different approaches were developed and they were applied to non-overlapping and overlapping regions to achieve depth map with low and high resolutions respectively. The overlapping case provides a depth map with a significantly higher resolution than the non-overlapping case with the caveat that it takes considerably more time to generate the results. For the sake of improving the efficiency of the overlapping case, the algorithm has been implemented using a parallel GPU solution based on the CUDA programming environment. As shown in section 3.3, the proposed algorithm provides excellent results and the depth map that is generated can be used to identify or segment any part of the cell in a straightforward manner and in particular the nucleus can be identified and an image showing a type of virtual staining can be generated. This algorithm is very useful for any application that requires the automatic identification of a cell nucleus for unstained cells using brightfield microscopy. The work presented in Chapter 3 is not directly used in the automated Raman system that is presented in Chapter 4. In Chapter 4, a simple image processing technique was employed based only on the global in-focus metrics that are investigated in Chapter 2. However, it may be possible to ensure more accurate alignment of the nucleus by incorporating the algorithm presented in this chapter into the automation process. This is considered to be a viable course of future work but insufficient time was available in this research masters to implement this. Finally, the work presented in this chapter is the subject of a jounral paper in preparation.

Chapter 4

Automated Raman Cytology System

In this chapter, an automated Raman micro-spectroscopy system that is capable of identifying unstained cells on a slide using image processing and automatically aligning the nuclei with the source laser for recording a spectrum is described. This work follows from the previous chapters where the methods of autofocusing was developed for unstained cells. The automation process is built around the open source Micro-manager software system and can be adopted by any lab using a commercial Raman micro-spectroscopy system or a custom built one. This methodology will help in the standardization of Raman cytology and its adoption into the clinic.

Raman spectroscopy can be used to evaluate the biomolecular composition of tissue and cell samples in a non-invasive manner. This technique is based on inelastic light scattering as a result of the interaction between incident monochromatic light and a biological sample. The majority of photons undergo elastic Rayleigh scattering whereby the emitted photons have the same energy to the incident photons. However, approximately one in 10^7 photons undergo inelastic Raman scattering[61], whereby the photon either gains energy (Anti-Stokes) or loses energy (Stokes) during this scattering process. The magnitude of the change in energy of the Raman photons is dependent on the rotational and/or vibrational energies of the molecules in the biological sample. By analyzing the shift in wavelength of the Raman photons, it is possible to infer information on the molecular composition of the sample being investigated. Specifically, the shift in wavelength of the photons and the magnitude of

the photons that have undergone this shift are indicative of a particular chemical bond and the concentration of that chemical bond respectively. For a complex mixture of different chemicals, such as in a biological sample, a highly varying Raman spectrum can be observed.

A basic Raman spectrometer is made up of four core components: (i) A suitable laser with a narrow linewidth is necessary to provide the excitation; (ii) A delivery system composed of a series of optical elements is required to transfer the excitation source to the sample; (iii) A collection system transfers the Raman scattered photons into a spectrograph. This collection system is once again made up of a series of optical elements, this time including an optical filter (such as a long pass or a notch filter) that is capable of attenuating the Rayleigh scattered photons while allowing the higher wavelength Raman scattered photons to pass through; (iv) The final component is the spectrograph. The entrance to the spectrograph is usually a slit that is imaged to a highly sensitive detector, via a diffraction grating that disperses the light into its constituent wavelengths. In a confocal Raman micro-spectrometer a Raman spectrometer is combined with a microscope; in this case both the delivery and collection systems make use of a microscope objective with a high numerical aperture. The microscope objective focuses the laser to a microscopic point on the sample and then efficiently collects the Raman scattered photons from this location. The point is imaged to a confocal aperture is in the collection path that selectively isolates the light emanating from the desired point on the sample and thereby reduces the background signal from the microscope objective and the sample substrate. Usually the microscope lamp must first be turned off before recording a spectrum. A more detailed description of a confocal Raman microspectrometer is given in Section 4.2.1.

Raman spectroscopy can be applied to analyze the molecular difference between various tissue and cell types. The first step in this process is usually to apply post-processing methods: (i) to reduce the background signal in the spectra; (ii) to calibrate the wavelength axis; (iii) to normalize the spectra; and (iv) to remove and smooth any cosmic rays. If subtle differences between similar datasets of spectra is wished to be identify, e.g. healthy and cancer cell types, multivariate statistical al-

gorithms may be applied following this post-processing. These algorithms enable the numerical classification of seemingly similar spectra, which enables the identification of an unknown cell type, given a database of spectra taken from known cell types. The method of Principal Component Analysis (PCA) followed by Linear Discriminant Analysis (LDA) is most commonly employed for the classification of diseased tissue or cells[62][63][64]. and this topic is discussed further in the following section.

The breakdown of this chapter is as follows. In Section 4.1, the basic physical principle of Raman micro-spectroscopy is introduced and its application to the classification of cell types. Two particular forms of cytology that can be augmented by Raman based classification are highlighted: namely screening for Cervical intraepithelial neoplasia (pap smear) and diagnosis of bladder cancer from samples of voided urine. In Section 4.2, a detailed description of the setup is provided and the methods on which the proposed automated Raman cytology system is based. In Section 4.3, a brief conclusion of this chapter is offered.

4.1 Raman Micro-spectroscopy for cell classification

4.1.1 Classification Algorithms

In order to identify the cell type associated with a particular Raman spectrum, the spectra obtained are initially subjected to pre-processing methods before undergoing further multivariate statistical analysis as discussed in the last sub-section. In the proposing automation algorithm, PCA, LDA and cross validation are employed for classification of cell types, but other techniques have also been demonstrated.

- Principal components analysis: PCA is a powerful statistical tool used to reduce the number of variables within a data set. To do this, PCA transforms the spectral data into a set of variables called principal components (PCs), whereby all PCs are orthogonal to each other and they are generated in such a way as to represent as much variance within the dataset as possible. Computationally, PCs are found by determining the covariance matrix of the data set, and calculating the eigenvectors

and eigenvalues of this covariance matrix. Further analysis can then be applied to these PCs to organize them into groups, or clusters, representing different cell or tissue pathologies; techniques such as LDA or logistic regression analysis (LRA) are often utilized.

- Linear discriminant analysis: LDA, also known as Fisher's discriminant analysis, is a supervised multivariate technique used to optimize class separability by finding the direction that provides the best separation for two or more groups of data. LDA is often applied to PC scores to further reduce the dimensionality of the data set. This is achieved by finding a linear combination of vectors that maximize the ratio of between-group variance and within-group variance[65]. By maximizing this ratio, LDA is able to provide the optimum separation for each group, thus improving classification results.

- Cross validation: Cross validation is often used to estimate how accurately the diagnostic model will perform. This is achieved by assessing the results of the statistical algorithm when applied to a validation set of data. The most commonly method is leave-one-out cross validation. Leave-one-out is based on using a single spectrum as the validation set, and the remaining spectra are used as the training set for the algorithm. This is repeated to test each spectrum in the dataset, and can be used to determine how accurate the model is at predicting the pathological status of the sample. Blind testing and double blind testing can also be applied[12]; these are based on concealing pathological information from the data in order to remove observer bias.

4.1.2 Application of Raman Micro-spectroscopy to Cancer Cell Classification

Raman micro-spectroscopy has been shown to be a powerful diagnostic method for the investigation of various cancer related diseases[66][67] including brain metastases[7], prostate[8], breast[9], esophagus[10], skin[11], bladder[12], oral[13], cervical[14] and lung[15] cancer. In many cases, the results have shown a significant increase in sensitivity and specificity for tissue and cell classification using Raman spectroscopy

when compared with other diagnostic approaches. This chapter is focused on the automation of Raman micro-spectroscopy for the analysis of epithelial cells. This automated system will have applications in the area of cytology, also known as cytopathology, which refers to the study of cellular disease and the diagnosis of disease by analyzing cellular changes. The most common example of this branch of pathology is the Pap smear[68] which can be used to screen for precancerous cervical lesions. Pap staining[69] is the multichromatic staining technique that used in this procedure to feature nuclear details and assure the transparency of cytoplasm. This staining method consists of a nuclear stain haematoxylin[70] and two counterstains OG-6 and Eosin Azure. Hydration prepares the cell sample for uptake of the nuclear dye; dehydration prepares the cell sample for uptake of the counterstains. Dehydration and clearing solutions result in cellular transparency and prepare the cell sample for the final steps: mounting and coverslipping. Generally, the purpose of Pap staining is to differentiate cells and reveal nuclei details. The nucleus of the cell is an important focal point for cytology. For a cancerous cell, the morphology of the nucleus can become larger and less uniform and it can appear darker. This physical change, resulting from altered DNA activity, can often be identified by qualitative inspection of microscopic images of the cell by a trained histopathologist. In many cases, staining is used to enhance the image contrast. In the paragraphs that follow in this subsection, the specific cases of cytopathology which have been shown to be improved using Raman micro-spectroscopy is highlighted. Although other forms of cytopathology are maybe expected to be benefit from Raman spectroscopy, these two branches are underlined as strong candidates for a fully automated Raman cytology system.

Approximately 471,000 women are diagnosed with invasive carcinoma of the cervix each year and 233,000 die from the disease worldwide[23]. Cervical cancer is preceded by a precancerous condition called Cervical Intraepithelial Neoplasia (CIN) that can be easily treated if detected. It is therefore important to identify CIN, which can be achieved using a screening test called a 'Pap smear'. An abnormal Pap smear is followed by colposcopic examination, biopsy and histological confirmation of the clinical diagnosis. This usually involves the visual examination of histological sections[62].

The grading characteristics are highly subjective and pre-malignancy may not be visually perceptible. A more recent innovation is the introduction of automated imaging systems (ThinPrep Imaging System or Focal Point Slide Profiler) that automatically scan the slide for large and dark nuclei which are features of abnormal cells. The Thinprep Imaging system has been shown be at least equivalent to manual screening[71]. In 1998, Mahadevan-Jansen and colleagues realized the potential use of near-IR Raman spectroscopy to distinguish cervical cytology grades[72]. They developed a compact fibre-optic probe to measure the in-vivo Raman spectra of cervical tissue[73]. Further studies have shown promising results for the application of this method in grading cervical pre-cancer [74]. In a recent study, a total of 1240 Raman spectra were acquired from 84 cervical patients. Confocal Raman micro-spectroscopy coupled with PCA-LDA modelling yielded a diagnostic accuracy of 84.1% (a sensitivity of 81.0% and a specificity of 87.1%) for in-vivo discrimination of dysplastic cervix[19].

Bladder cancer is the fourth most common cancer in men, with about 74,690 new cases of bladder cancer diagnosed in 2014 in the United States[75]. Cystoscopy is the most widely used diagnostic method within present clinical techniques, whereby a small tube is inserted into the bladder through the urethra to examine the lining of the bladder and urethra. Cytoscopic identification of bladder cancer has a sensitivity and specificity of between 62% - 84% and 43% - 98% [22]. Cystoscopy has a number of disadvantages; firstly it is inherently an invasive procedure and secondly it produces a significant number of false negatives due to the abnormal appearance of the urothelium in patients with inflammation, which makes the identification of carcinoma in situ problematic. Urine cytology, whereby microscopic images of epithelial cells that have been retrieved from urine samples are qualitatively inspected has been shown to be a useful adjunct for bladder cancer diagnosis[76]. While it has the obvious advantage of being entirely non-invasive, it only achieves a high sensitivity and specificity for high grade cancers. The sensitivity reduces significantly for low grade cancers, which represent the majority of cases[77]. Recently it has been shown that standard bladder cytology, which has a 80% to 90% sensitivity and 98% to 100% specificity for high grade[20] and 20%-50% sensitivity for low grade cancer[21] can

be significantly improved using Raman micro-spectroscopy to achieve 92% sensitivity and 91% specificity for low grade and 100% sensitivity for high grade bladder cancer[12][22]. Clearly, Raman cytology has a strong potential to become a standard clinical diagnostic technique.

One important reason that explains why Raman micro-spectroscopy has not yet become an everyday clinical tool for disease diagnosis and cell classification is that there exists a lack of consistency and standardization in terms of equipment, consumables, and methodologies across different research groups, which results in considerably varying spectra. One solution that may help to mitigate the lack of standardization could be to implement a fully automated Raman cytology system thereby minimizing user variability. In addition, a higher throughput of cellular analysis could be expected from such a system and with a reduction in manpower and cost.

4.2 Automated Raman Cytology

4.2.1 Experimental set-up for automated Raman

Conventional Raman micro-spectroscopy involves the use of a microscope and a confocal aperture in order to isolate the Raman spectrum from a specific microscopic three-dimensional point in a specimen. The laser beam can be delivered at 180° to the sample surface or at 90°, in either a back scattering- or transmission-based system. Biological samples can be measured both in vitro and ex vivo with this method by mounting them onto a substrate.

Fig. 4-1 illustrates the system for automated Raman micro-spectroscopy that has been custom built in the lab. A state of the art Raman microscope will cost in the order of at least $100,000 (can be much more) but an equivalent one can be built from basic elements for less than half this amount.

The basic optical design in the lab is as follows; The delivery path (red path in Fig. 4-1) begins with a laser with a sufficiently narrow bandwidth (Sacher Laser TEC 520 7080-100, wavelength 785 nm, power 120 mW) first passing through a computer

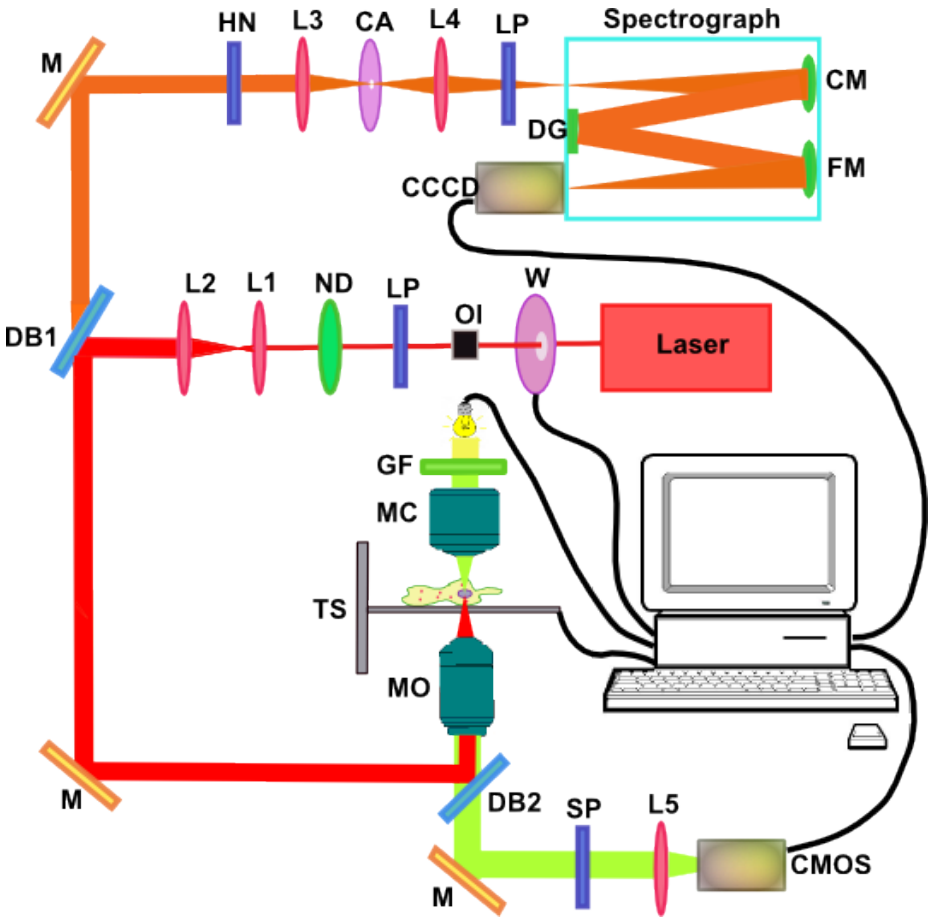

Figure 4-1: Automated Raman cytology system setup

controlled filter wheel. The reason for this filter wheel is to allow blocking or reduction of the laser when performing image capture and image processing which constitutes a core component of the automation process. An electronic shutter or iris could perform the same function. Following the filter wheel, an optical isolator OI (Sacher Laser, ISO-35-0780) ensures elimination of any back reflections from the set-up that may return into the laser cavity and damage the laser head. A line pass filter LP (Semrock LL01 785-12.5) is placed after the isolator, which removes any spurious lines from the laser. Only the line at 785nm is allowed to reach the neutral density filter ND (Edmund Optics) which can be rotated enabling the power of the laser beam to be varied. This is followed by two lenses, L1 and L2 (Thor Labs), that are used to expand the laser beam such that the diameter of the collimated beam is approximately equal to the back aperture of the microscope objective MO (UMPlanFl 50x/0.85)

The collimated beam is directed onto a dichroic beam splitter DB1 (Semrock LPD01-785RS) which reflects light at 785 nm but transmits higher wavelengths. This facilitates reflection of the laser beam into the microscope while allowing the backscattered Raman photons to pass through towards the spectrograph. DB1 reflects the beam towards a mirror, M (MaxMirror), and then onto a second dichroic mirror, DB2, which relects all wavelengths above 650 nm and transmits all shorter wavelengths. DB2 is carefully aligned such that it reflects the beam directly into the back of the microscope objective. The microscope objective is chosen such that it has a high numerical aperture which is important for delivering a tightly focused illumination spot and for recovering as many Raman backscattered photons as possible. It is also important that the microscope objective efficiently transmits light in the NIR as this will also impact on the system to recover a strong Raman signal; plan fluorite microscope objectives provide good performance. The microscope objective focuses the beam to a tightly focused spot on the sample S approximately 1-2μm in diameter. The sample is placed on a translation stage, TS (ASI, LS-2000 and LS-50), that enables sample positioning relative to the laser spot. For the application of cellular classification, it is desirable to position the cell such that the spot is located within the cell nucleus as this results in optimum classification sensitivity.

The collection path (shown in orange in Fig. 4-1) originates at the sample plane where the backscattered Raman photons (785-1050 nm) travel back through the microscope objective, are reflected by DB2 and then pass through the dichroic beam splitter DB1. A holographic notch filter HN (Kaiser HNF-785.0-1.0) is used to remove Rayleigh scattered light at 785 nm that has passed through the dichroic beam splitter while simultaneously transmitting all other wavelengths. A third lens L3 (Thor Labs) focuses the light to a 100μm confocal aperture CA (Thor Labs) that is used to ensure that light reaching the spectrograph has originated from a three dimensional point within the object in the order of 1μm in all three dimensions, thereby enabling 3D localization of the Raman signal from the sample. The lens L4 (Thor Labs) forms a one-lens imaging system from the plane of the confocal aperture to the plane of the entrance slit SL of the spectrograph (Andor Shamrock 500), which provides 0.25 magnification, thereby ensuring that the spot size entering the spectrograph is equal to the pixel pitch of the spectrograph camera (25μm). The system was designed such that the angle of light entering the spectrograph is matched to the f number of the spectrograph (6.5). A long pass filter, LP (Semrock LP02-785RU-25), is placed near the entrance slit in order to further reduce any Rayleigh scattered/laser light that has reached the spectrograph. The image of the slit is projected onto a cooled electron multiplying CCD camera CCCD (Andor DU420A-BRDD) via a collimating mirror CM, a diffraction grating DG, and a focusing mirror FM. Each row of pixels records an image of the slit corresponding to a specific wavelength, and in this way the Raman spectrum is recorded using the Andor Solis software system. It is important to use a high quantum-efficiency, low-noise, cooled CCD in order to recover the weak Raman signal with minimal noise.

Independently, a separate imaging path shown in green in Fig. 4-1, allows the sample to be imaged directly onto a second digital camera. A 100-W halogen lamp passes through a green filter GF (Nikon) and then through an Abbe condenser MC (Nikon) which focuses the light onto the sample and into the microscope objective. Since the green light has a wavelength less than 650 nm, the light passes through DB2 and then through a short pass filter SP (Semrock FF01-775/SP-25), which is designed

to transmit all wavelengths shorter than 775 nm thereby blocking the laser light. The lens L5 images the object plane onto a digital camera, DC (Basler acA2000âĂŞ340km with 1088×2040 pixels with size 5.5μm in both dimensions), that is fixed to the front exit port of the microscope. This short pass filter can be removed if the laser spot imaged onto the camera is wished to be seen, which can be useful for one form of automation mentioned below; it has been found that the optimal scattering plane can be determined by processing images of the sample where the laser illumination spot is visible. However, it is possible to determine this optimal plane in other ways, thereby allowing SP to be utilized and thus removing the need for the filter wheel, W, to eliminate the presence of the laser spot when capturing images of the sample. This is regarded as a subject for further study.

4.2.2 Method of Automation

In the proposing automated system, the following elements are controlled using a single software package:

- The microscope halogen lamp can be switched on and off electronically . The lamp must be turned on for imaging the cells and automatic alignment of the cells with the laser but it must be turned off when recording a Raman spectrum as some of the light will make its way to the spectrograph and swamp the Raman signal.

- A filter wheel, W, or electronic shutter is used to block the laser when recording images of the cells on the digital camera. The laser must be on when recording a spectrum but it must be turned off when recording images of cells to be used in the image processing algorithms as part of the overall automation process.

- The CMOS digital camera can record images of the sample.

- The cooled CCD camera can record spectra.

- The xyz translation stage can be controlled electronically to align a cell following from image processing algorithms.

- The angle of the grating in the spectrograph can be controlled in order to change the wavelength range that is recorded. It is also possible to change the grating itself if different resolutions/spectral bandwidths are required.

- In this chapter, a method that entails one manual step involving a change in microscope objective is described. This enables changing from low to high magnifications at different stages of the automation process. It is possible for the microscope objective to be changed automatically using an electric turret wheel on a motor.

The automation process consists of a number of steps that are illustrated in Fig. 4-2. All of these steps are implemented using a single software package called Micromanager[24] which can integrate all of the hardware and software that is discussed in the previous section. The initial series of steps, shown on the left side of Fig. 4-2, are applied using a lower magnification objective; in this case a Nikon x20 plan fluor objective is used. This allows us to scan a relatively large field of view on the slide which facilitates an automated selection process where cells are chosen for Raman spectroscopy based on some quality metric. All images recorded using x20 magnification result in an equivalent pixel size of $0.275\mu m$ in both of the in-plane dimensions, x and y. This value of effective pixel size decreases by a factor of 5 times when the microscope objective is switched to the x100 magnification which gives $0.055\mu m$.

The initial set of operations are implemented at x20 magnification and the processes begin by manually choosing a good starting position (x_0, y_0, z_0).(x_0, y_0) is arbitrary so long as the chosen area has enough candidate cells and is not very close to the edge of the substrate. For full automation, the centre of the substrate can simply be selected but basic manual alignment to an area with cells will speed up the overall process. However, the initial position in the z direction, z_0, is required to be the global in-focus plane. This can be automated using a basic autofocus algorithm[44]. Once (x_0, y_0, z_0) is selected, the following process in x20 magnification is automatically performed using a script written in Micromanager. The initial steps are designed for the

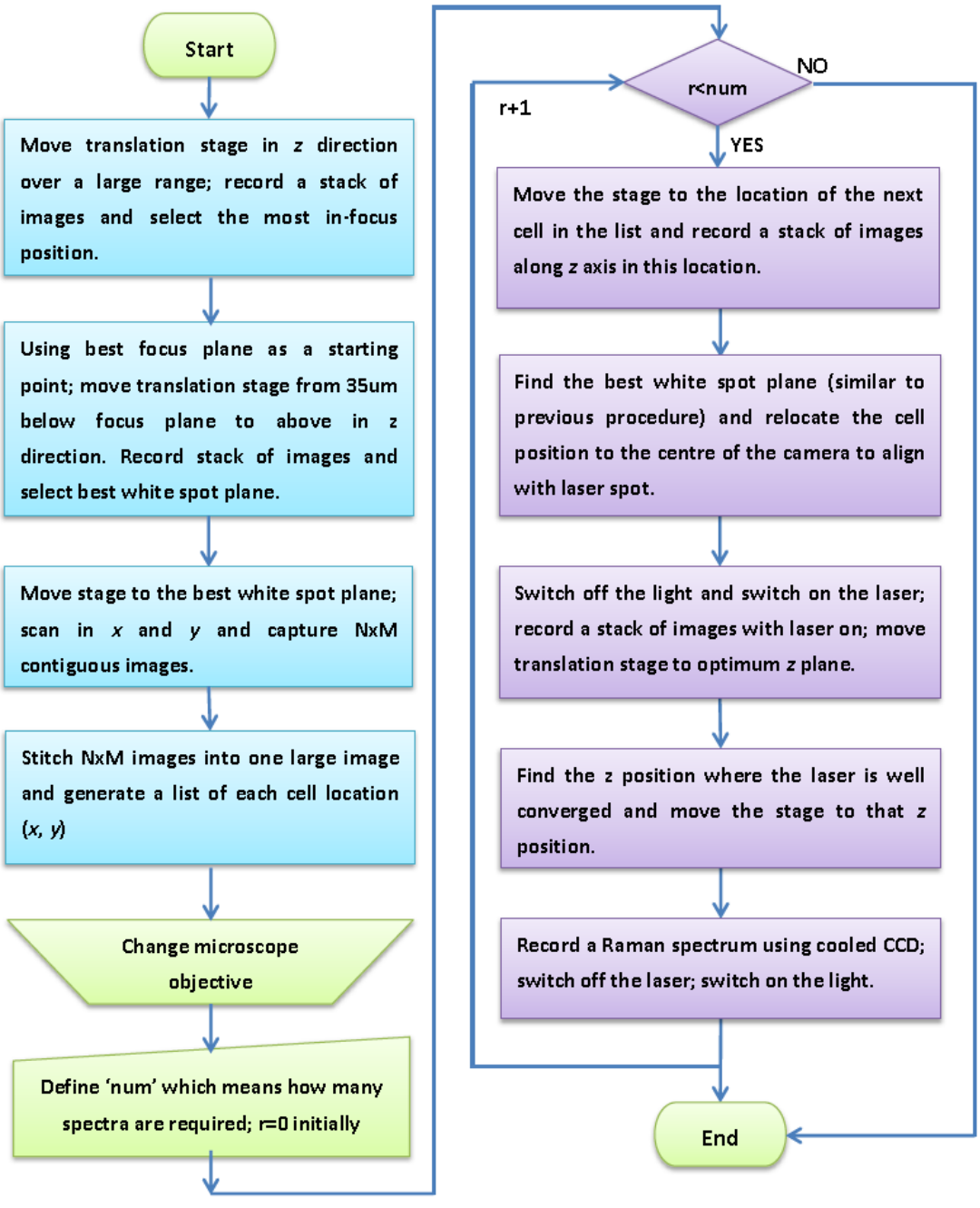

Figure 4-2: Flow chart of automation process.

purpose of quickly scanning a relatively large field of view in order to identify good candidate cells from all of the cells in the field. At the end of the first stage, a list of coordinates of suitable cells are generated according to some metric. Suitable metrics include (but are not limited to) the following:

- The distance between neighbors whereby the cell that is most distant from its neighbors (i.e. most isolated cell) will rank first. This can enable us to be sure that cells are not overlying one another which can result in problems in spectra recording. This is the metric that is applied in the experimental validation presented here.

- Some other aspects of morphology eg. the overall cell size, the nucleus size or the cytoplasm to nuclues ratio. These values could be determined using other segmentation algorithms that are not discussed here or they could be inferred in some way from the bright spots that are described below.

- The appearance of new cells in a particular area if a sequence of images are captured with cell growth occuring between captures. Such new cells could be quickly identified using the bright spot methodology described below.

The nucleus of cells are often spherical or ellipsoidal in shape and are more dense that the surrounding cytoplasm. One effect of this morphology is that the cell effectively behaves like a small crude lens that approximately focuses the microscope illumination to a point spot at a short distance below the cell (assuming an inverted microscope configuration.). This lens effect leads to the appearance of bright white spots in a plane that is slightly below the image focus plane for an inverted microscope (slightly above for an upright microscope.) The (x,y) location of this spot indicates the (x,y) location of the nucleus. An example of this effect is provided in Fig. 4-3 below. The experimental parameters need to be described here: bladder cell line T24, x20 magnification, Basler camera. The z shift between image (a) and (b) in μm.

Similar methods have previously been applied to count unstained cells using brightfield microscopy. In Ref. [40] the spatial coherence of the source illumination

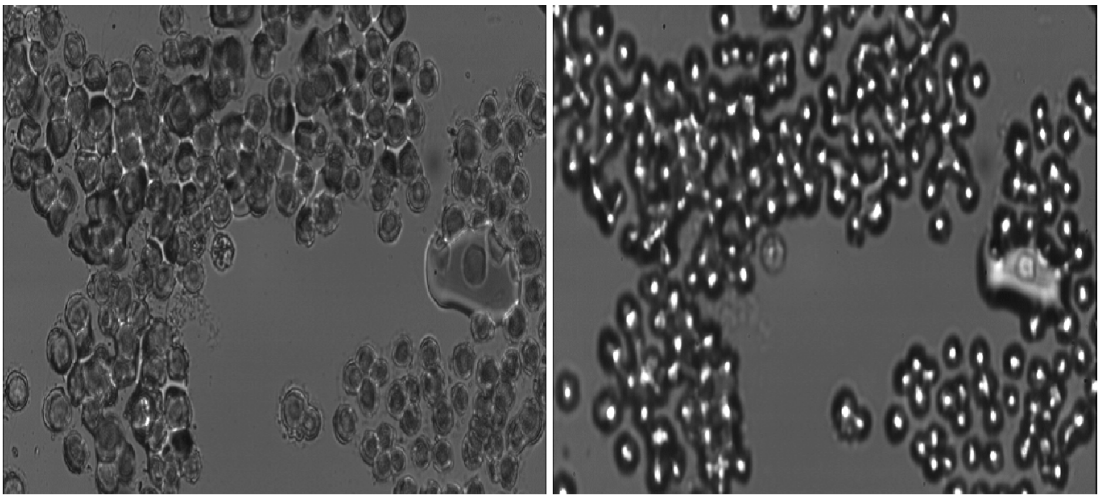

Figure 4-3: Unstained bladder epithelial cells on a Calcium Fluoride slide shown in-focus on the left image and a slightly out of focus image is shown on the right. The bright spots in the image approximately overly the centres of the nuclei of the cells. The sizes of microscope images shown above are identical which is 280.5μm (width)$\times$149.6μm (height).

was considered to be an important factor in the appearance of the spots. However, It has been found that for the cells have been investigated, standard Kohler illumination provides satisfactory results. To choose the best white spot plane automatically, a stack of images along the vertical direction is firstly recorded and saved starting from a position $35\mu m$ below the focal plane with a step size of $2.5\mu m$. In total, 30 steps are taken; 14 images are below the focal plane and 15 images above. The variance of each image is calculated in order to find the maximum value which corresponds to the plane which is considered to have the optimally bright spots that can be used in the subsequent processing steps. The plot of image variance versus z position is shown in Fig. 4-4. The stage is then moved to the plane resulting in the maximum image variance.

For the steps shown on the left side of flowchart in Fig. 4-2, only the x20 magnification is employed and the z position of the translation stage remains unchanged. The stage is scanned in the x and y directions in order to record a grid of contiguous images. In practice, some overlap between the images are required in order to facilitate stitching into a larger image. In the example presented in Fig. 4-5 3x3 images were recorded by moving translation stage $14.96\mu m$ up or down and $28.05\mu m$ left

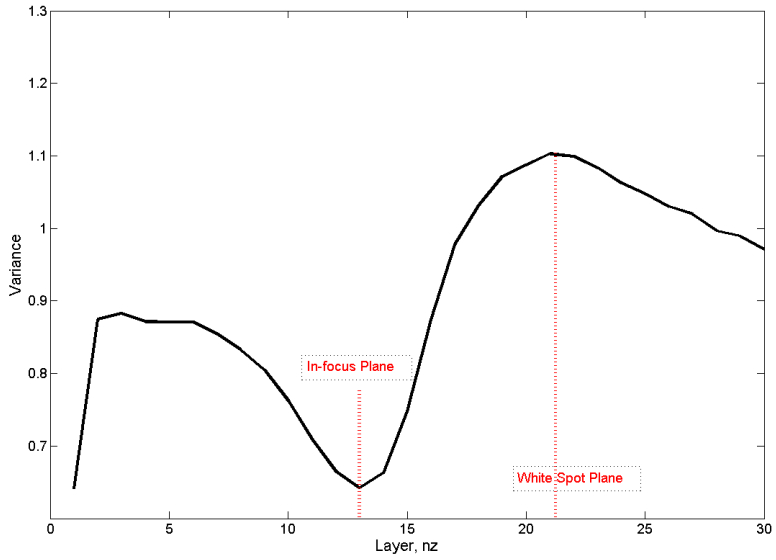

Figure 4-4: Variance plot for the stack of images in the vertical direction. The maximum value corresponds to the plane with the optimally bright spots, which is then used for locating cell nuclei.

which corresponds to the half image height and width respectively. These nine images are then stitched together using a correlation algorithm[12]. The result of stitching these images together is to create a larger image of approximately 2176×4096 pixels which corresponds to an area of $0.25mm \times 0.5mm$ in size, which covers a large portion of the cells on investigated slide. From this large image, the positions of the local maxima is detected in the image where a threshold is included in order to make sure that only suitably bright spots are targeted. In this way, the approximate horizontal coordinates of the cell nuclei can be identified. The cells are then ranked according to some metric as discussed above. In this case, cell candidates are ranked according to isolation, thereby ensuring that manually overlying cells are not included, the spectra of which may be corrupted. The process is illustrated in Fig. 4-5.

In the second stage of the automation process, the microscope objective is changed from from x20 to x100 magnification and immediately an autofocus algorithm is applied to again detect the best focal plane. The automation algorithm now moves the stage to the coordinate of the first cell in the list. A minor adjustment is necessary to relocate the target cell nucleus to the center of the laser spot due to an offset in

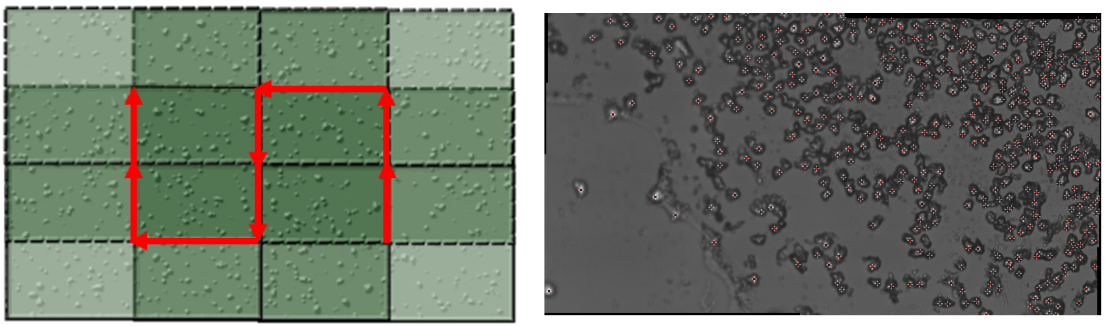

(a) (b)

Figure 4-5: (a) Illustration of the recording of a grid of images with 50% overlap. In this example nine overlapping images are recorded (8 shifts are shown); (b) The larger image made up of the nine record images. This stitched image size is 561μm (width)$\times$299.2μm (height). All of the cell nuclei are found using the bright spot method, as shown using the red targets.

the experimental setup that is brought about by changing the microscope objective. To align correctly, a stack of images along the z axis is recorded and saved, once again using a step size of 2.5μm and again the image corresponding to the maximum variance is found in order to determine the best white spot plane. The stage is moved to align the white spot with the laser spot. The horizontal position of the stage is now correctly aligned but the z position is not yet ideal for recording a Raman signal of the cell nucleus. Two options are presented for optimal z positioning:

- The best z position of the cell nucleus can be empirically determined using the most in focus plane and/or the white spot plane as a reference. This can be achieved by recording a Raman spectrum for a stack of different z positions, using a relatively short exposure time of approximately 5 seconds and qualitatively deciding best spectrum. This could be repeated for a number of different cells and the best z position, relative to the focal plane or the white spot plane, can be empirically estimated in this way. The optimal position can then be used for each new cell using the most in-focus plane and/or the white spot plane as a reference. Alternatively the procedure could be repeated for every cell, where a relatively short exposure time is used to record a series of images in the z direction; the best z position could be decided by quantitatively inspecting each recorded spectrum and deciding on the best one by applying a simple criteria

based on expected cell peaks. Once the best z position is determined, a longer exposure time can be used in this position.

- The microscope lamp can be automatically switched off and the laser can be automatically switched on . Then a stack of images can be recorded and observe the scattering of the laser spot for different z positions. The z position corresponding to the least amount of scattering is the optimal plane; see Fig. 4-6. This plane can be identified again using variance or mean value. This is the method we employed in the example presented here.

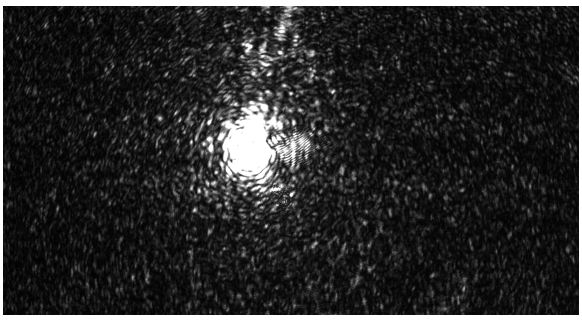

Figure 4-6: Image of the laser spot at the z position resulting in least scattering. This image size is 56.1μm (width)$\times$29.92μm (height).

Once alignment in all three dimensions has been achieved, the alogirthm switches off the microscope lamp, switches on the laser and records a spectrum for a predefined exposure time using the cooled CCD camera. An additional step that could be included to test the quality of the spectrum and to decide whether or not to save or record another spectrum. Finally, the laser is switched off using the filter wheel, the lamp is turned on and the xy stage moves the slide to the position of the second cell on the list. The process is repeated until some pre-defined number of cells are investigated or there are no more cells on the list. Finally, when all of the spectra have been recorded, an algorithm to reduce the background[78][79], remove cosmic rays[80], and to area normalize is automatically applied. The code for preprocessing is written in matlab which is automatically called from the Micromanager script.

4.3 Conclusion

In this chapter, an automated Raman cytology system built around the Micromanager software system was introduced which integrates various hardware and software components including an autofocusing algorithm that was proposed in Chapter 2 and a number of image processing steps. The experimental validation using several cell lines is currently being investigated at the time of writing this thesis. The content of this chapter is the subject of a journal paper in preparation.

Chapter 5

Conclusion and Future perspectives

In this thesis, an automated Raman cytology system has been developed which is built around the open source Micro-manager software system. This system is made up of a conventional confocal Raman micro-spectroscopy system and controls a translation stage, an illumination lamp, a filter wheel, a spectrograph, and two cameras that are connected to the computer. Automation is realised by scanning a slide and recording a series of images using standard brightfield microscopy; the images are then stitched together to form a large mosaic, which is then input to an image processing algorithm that is capable of identifying the cell positions and recording them for further analysis. The nucleus of cell provides the most reliable spectrum for diagnostics and proposed algorithm is capable of identifying the nucleus without the need for staining. The process involves a number of image processing algorithms for autofocusing, image stitching and for identification of approximate centre of the cell nucleus.

Chapter 2, an analysis of autofocusing algorithms was provided for unstained cells by investigating 15 commonly used autofocus metrics that have been previously applied to stained or fluorescent cell images. For the first time that the position of the global minimum on the autofocus curve corresponds to the correct focal plane is identified for unstained cells instead of the position of the global maximum which is the well known case for opaque objects. The reason for this is that the unstained cells are described by an approximately phase-only transmission function and they appear effectively transparent when they are in-focus and in this plane there exists very little

image contrast; however, as moving away from this focal plane, either above or below, high contrast features appear in the image. These high contrast out-of-focus details result from the effect of a phase-only function that is propagated a short distance. A simple example of this is the imaging of a lens; imaging of the lens plane will provide an image with no detail but the image of the focal plane of the lens will contain a a region of focused light, assuming a light source is behind the lens. This example is not chosen arbitrarily. The nucleus of a cell behaves like a miniature lens and approximately focuses the microscope illumination to a crude bright spot in a plane that is a short distance from the correct image plane. This effect is used to identify the positions of the cell nuclei, which in turn facilitates optimal alignment of the cells with the source laser for Raman micro-spectroscopy. It has been determined that the best plane to image these "bright spots" can be located at the maximum value of certain autofocus metrics which further simplifies the overall process. In Chapter 3, an algorithm was presented for recovering the 3D morphology of a cell using brightfield microscopy, where once again the autofocus metrics that were investigated in Chapter 2 are used. In this case, a stack of images in recorded where the slide is moved along the vertical axis and the metrics are applied to sub-regions in the image planes. In this way, the most in-focus depth for each smaller region can be determined and a depth map of the cell can be estimated. Two algorithmic approaches were demonstrated with different advantages in terms of computational time and spatial resolution and the more intensive case was implemented using GPU processing in order to speed up the overall process by almost two orders of magnitude. At the time of writing this thesis, this algorithm hasn't been incorporated into proposed automation procedure, but it should be envisaged that more accurate cell alignment could be achieved by doing so and this is considered to be a viable route for future research. We believe after recording a set of spectra, cosmic ray removal algorithm, background subtraction algorithm and classification algorithm like PCA and LDA can be applied afterwards to get diagnostic results.

At the time of writing this thesis, the research is in the stage of testing proposed automated Raman cytology system on a number of cell lines, but this work is not

sufficiently complete for presentation in this thesis. Over the coming weeks, we hope to complete experimental work and to test and validate the automated Raman cytology system on a number of bladder cancer and breast cancer cell lines in order to achieve high sensitivities and specificities for each case using PCA and LDA. In future work, we would like to combine the 3D morphology algorithm with the automation system for superior nucleus alignment and we would also like to test the proposing system on patient samples for a true diagnostic test. In the longer term, we envisage the development of more sophisticated image processing algorithm that may be capable of distinguishing between different cell types in the image for a more targeted approach. Such an algorithm is necessitated by the presence of other cell types in bladder and cervical cytology, e.g. blood cells. We are also considering the development of a digital holographic microscope that is built around the existing confocal Raman micro-spectrometer that would be capable of providing very reliable information on cell shape and morphology.

Bibliography

[1] Derek Albert Long and DA Long. *Raman spectroscopy*, volume 206. McGraw-Hill New York, 1977.

[2] Michael Mazilu, Anna Chiara De Luca, Andrew Clive Riches, Charles Simon Herrington, and Kishan Dholakia. Optimal algorithm for fluorescence suppression of modulated raman spectroscopy. *Optics Express*, 18(11):11382 – 11395, 2010.

[3] Judith B Snow, Shi-Xiong Qian, and Richard K Chang. Stimulated raman scattering from individual water and ethanol droplets at morphology-dependent resonances. *Optics letters*, 10(1):37–39, 1985.

[4] A.T. Tu. *Raman spectroscopy in biology: principles and applications*. A Wiley-Interscience publication. Wiley, 1982.

[5] Ludwig Fahrmeir, Gerhard Tutz, and Wolfgang Hennevogl. *Multivariate statistical modelling based on generalized linear models*, volume 2. Springer New York, 1994.

[6] Andrea Molckovsky, Louis-Michel Wong Kee Song, Martin G. Shim, Norman E. Marcon, and Brian C. Wilson. Diagnostic potential of near-infrared raman spectroscopy in the colon: Differentiating adenomatous from hyperplastic polyps. *Gastrointestinal Endoscopy*, 57(3):396 – 402, 2003.

[7] Leanne M. Fullwood, Graeme Clemens, Dave Griffiths, Katherine Ashton, Timothy P. Dawson, Robert W. Lea, Charles Davis, Franck Bonnier, Hugh J. Byrne, and Matthew J. Baker. Investigating the use of raman and immersion raman spectroscopy for spectral histopathology of metastatic brain cancer and primary sites of origin. *Anal. Methods*, 6:3948–3961, 2014.

[8] Rachel E. Kast, Stephanie C. Tucker, Kevin Killian, Micaela Trexler, Kenneth V. Honn, and Gregory W. Auner. Emerging technology: applications of raman spectroscopy for prostate cancer. *Cancer and Metastasis Reviews*, pages 1–21, 2014.

[9] Abigail S. Haka, Zoya Volynskaya, Joseph A. Gardecki, Jon Nazemi, Robert Shenk, Nancy Wang, Ramachandra R. Dasari, Maryann Fitzmaurice, and Michael S. Feld. Diagnosing breast cancer using raman spectroscopy: prospective analysis. *Journal of Biomedical Optics*, 14(5), 2009.

[10] Bergholt MS, Zheng W, Lin K, Ho KY, Teh M, Yeoh KG, So JB, and Huang Z. In vivo diagnosis of esophageal cancer using image-guided raman endoscopy and biomolecular modeling. *Technol Cancer Res Treat*, 10:103–112, 2011.

[11] Lui H, Zhao J, McLean D, and Zeng H. Real-time raman spectroscopy for in vivo skin cancer diagnosis. *Cancer Res*, 72(10).

[12] Laura T. Kerr, Katarina Domijan, Ivor Cullen, and Bryan M. Hennelly. Applications of raman spectroscopy to the urinary bladder for cancer diagnostics. *Photonics & Lasers in Medicine*, 3:193–224.

[13] S. P. Singh, Atul Deshmukh, Pankaj Chaturvedi, and C. Murali Krishna. In vivo raman spectroscopy for oral cancers diagnosis. *Proc. SPIE*, 8219, 2012.

[14] Cervical cancer detection based on serum sample raman spectroscopy. *Lasers in Medical Science*, 29(3):979–985, 2014.

[15] Zhiwei Huang, Annette McWilliams, Harvey Lui, David I. McLean, Stephen Lam, and Haishan Zeng. Near-infrared raman spectroscopy for optical diagnosis of lung cancer. *International Journal of Cancer*, 107(6):1047–1052, 2003.

[16] E. D. P. De Robertis, W. W. Nowinski, and Francisco A. Saez. General cytology. *The Anatomical Record*, 108(2):333–334, 1950.

[17] Steven J. Choquette, Edgar S. Etz, Wilbur S. Hurst, Douglas H. Blackburn, and Stefan D. Leigh. Relative intensity correction of raman spectrometers: Nist srms 2241 through 2243 for 785 nm, 532 nm, and 488 nm/514.5 nm excitation. *Appl. Spectrosc.*, 61(2):117–129, Feb 2007.

[18] Virginia A. Moyer and U.S. Preventive Services Task Force. Screening for cervical cancer: U.s. preventive services task force recommendation statement. *Annals of Internal Medicine*, 156(12):880–891, 2012.

[19] Shiyamala Duraipandian, Wei Zheng, Joseph Ng, Jeffrey J. H. Low, Arunachalam Ilancheran, and Zhiwei Huang. Near-infrared-excited confocal raman spectroscopy advances in vivo diagnosis of cervical precancer. *Journal of Biomedical Optics*, 18(6), 2013.

[20] Debby Chao, Stephen J Freedland, Allan J Pantuck, Amnon Zisman, Arie S Belldegrun, and FACS. Bladder cancer 2000: Molecular markers for the diagnosis of transitional cell carcinoma. *Rev Urol*, 3(2):85–93, Jun 2001.

[21] Hughes JH, Raab SS, and Cohen MB. The cytologic diagnosis of low-grade transitional cell carcinoma. *Am J Clin Pathol*, 114:59–67, 2000.

[22] Amos Shapiro, Ofer. N. Gofrit, Galina Pizov, Jeffrey Kirk Cohen, and John Maier. Raman molecular imaging: A novel spectroscopic technique for diagnosis of bladder cancer in urine specimens. *European Urology*, 59(1):106 – 112, 2011.

[23] J. Blackledge, D. Dubovitskiy, and F Lyng. Targeting cell nuclei for the automation of raman spectroscopy in cytology, 10 2014. WO Patent App. PCT/EP2013/070,495.

[24] Arthur Edelstein, Nenad Amodaj, Karl Hoover, Ron Vale, and Nico Stuurman. *Computer Control of Microscopes Using Micro–manager*. John Wiley & Sons, Inc., 2010.

[25] J.L. Pech-Pacheco, G. Cristobal, J. Chamorro-Martinez, and J. Fernandez-Valdivia. Diatom autofocusing in brightfield microscopy: a comparative study. In *Pattern Recognition, 2000. Proceedings. 15th International Conference on*, volume 3, pages 314–317 vol.3, 2000.

[26] F. Zernike. Phase contrast, a new method for the microscopic observation of transparent objects. *Physica*, 9(7):686–698, July 1942.

[27] Florian Charrière, Anca Marian, Frédéric Montfort, Jonas Kuehn, Tristan Colomb, Etienne Cuche, Pierre Marquet, and Christian Depeursinge. Cell refractive index tomography by digital holographic microscopy. *Opt. Lett.*, 31(2):178–180, Jan 2006.

[28] Tristan Colomb, Frédéric Montfort, Jonas Kühn, Nicolas Aspert, Etienne Cuche, Anca Marian, Florian Charrière, Sébastien Bourquin, Pierre Marquet, and Christian Depeursinge. Numerical parametric lens for shifting, magnification, and complete aberration compensation in digital holographic microscopy. *J. Opt. Soc. Am. A*, 23(12):3177–3190, Dec 2006.

[29] D Murphy. Numerical parametric lens for shifting, magnification, and complete aberration compensation in digital holographic microscopy. *Fundamentals of Light Microscopy and Digital Imaging*, 23(12):158–168, 2001.

[30] A. Diaspro. *Optical Fluorescence Microscopy: From the Spectral to the Nano Dimension*. Springer-Verlag Berlin Heidelberg, 2010.

[31] Melvyn Folkard, Kevin M Prise, Geoff Grime, Karen Kirkby, and Borivoj Vojnovic. The use of microbeams to investigate radiation damage in living cells. *Appl Radiat Isot*, 67(3):436–9, 2009.

[32] Anna Mölder, Mikael Sebesta, Mats Gustafsson, Lennart Gisselson, Anette Gjörloff Wingren, Kersti Alm, and Lennart Gisselsson. Non-invasive, label-free cell counting and quantitative analysis of adherent cells using digital holography. *Journal of Microscopy*, 232:2, s. 240-247, 2008.

[33] Russell RA, Adams NM, Stephens DA, Batty E, Jensen K, and Freemont PS. Segmentation of fluorescence microscopy images for quantitative analysis of cell nuclear architecture. *Biophysical Journal*, 96:3379–89, Apr 2009.

[34] Jyrki Selinummi, Pekka Ruusuvuori, Irina Podolsky, Adrian Ozinsky, Elizabeth Gold, Olli Yli-Harja, Alan Aderem, and Ilya Shmulevich. Bright Field Microscopy as an Alternative to Whole Cell Fluorescence in Automated Analysis of Macrophage Images. *PLoS ONE*, 4(10), October 2009.

[35] Shutong Tse, Laura Bradbury, Justin W.L. Wan, Haig Djambazian, Robert Sladek, and Thomas Hudson. A combined watershed and level set method for segmentation of brightfield cell images. *Proc. SPIE*, 7259:72593G–72593G–10, 2009.

[36] Felix Buggenthin, Carsten Marr, Michael Schwarzfischer, Philipp S. Hoppe, Oliver Hilsenbeck, Timm Schroeder, and Fabian J. Theis. An automatic method for robust and fast cell detection in bright field images from high-throughput microscopy. *BMC Bioinformatics*, 14:297, 2013.

[37] Firas Mualla, Simon Scholl, Bjorn Sommerfeldt, Andreas K. Maier, and Joachim Hornegger. Automatic cell detection in bright-field microscope images using sift, random forests, and hierarchical clustering. *IEEE Trans. Med. Imaging*, 32(12):2274–2286, 2013.

[38] Rehan Ali, Mark Gooding, Tunde Szilagyi, Borivoj Vojnovic, Martin Christlieb, and Michael Brady. Automatic segmentation of adherent biological cell boundaries and nuclei from brightfield microscopy images. *Mach. Vision Appl.*, 23(4):607–621, July 2012.

[39] Marko Tscherepanow, Frank Zollner, and Franz Kummert. Industrial conference on data mining - workshops. page 86.

[40] L Louis Drey, Michael C Graber, and Jan Bieschke. Counting unstained, confluent cells by modified bright-field microscopy. *Biotechniques*, 55(1):28–33, 2013.

[41] Francois Aguet, Dimitri Van De Ville, and Michael Unser. Model-based 2.5-d deconvolution for extended depth of field in brightfield microscopy. *IEEE Transactions on Image Processing*, 17(7):1144–1153, 2008.

[42] Hahn K Shen F, Hodgson L. Digital autofocus methods for automated microscopy. *Methods in Enzymology*, 414:620–32, 2006.

[43] Rafael Redondo, Gloria Bueno, Juan Carlos Valdiviezo, Rodrigo Nava, Gabriel Cristobal, Oscar Deniz, Marcial Garcia-Rojo, Jesus Salido, Maria del Milagro Fernandez, Juan Vidal, and Boris Escalante-Ramirez. Autofocus evaluation for brightfield microscopy pathology. *Journal of Biomedical Optics*, 17(3):036008–1–036008–8, 2012.

[44] Shu Yu Wu, Nazim Dugan, and Bryan M. Hennelly. Investigation of autofocus algorithms for brightfield microscopy of unstained cells. *Proc. SPIE*, 9131, WA 2012.

[45] H Netten, I T Young, L J van Vliet, H J Tanke, H Vroljik, and W C Sloos. Fish and chips: automation of fluorescent dot counting in interphase cell nuclei. *Cytometry*, 28(1):1–10, 1997.

[46] Richard A. Muller and Andrew Buffington. Real-time correction of atmospherically degraded telescope images through image sharpening. *J. Opt. Soc. Am. A*, 64(9):1200–1210, 1974.

[47] Groen F.C, Young I.T, and Ligthart G. A comparison of different focus functions for use in autofocus algorithms. *Cytometry*, 6(2):81–91, 1985.

[48] T. Yeo, S.O. Jayasooriah, and R. Sinniah. Autofocusing for tissue microscopy. *Image and Vision Computing*, 11:629–639, December 1993.

[49] Eric Krotkov. Focusing. volume 1, pages 223–237, October 1988.

[50] D. Vollath. Automatic focusing by correlative methods. *Microscopy*, 147(3):279–288, 1987.

[51] D. Vollath. The influence of the scene parameters and of noise on the behaviour of automatic focusing algorithms. *Microscopy*, 151(2):133–146, 1988.

[52] J. M. Geusebroek, F. Cornelissen, A. W. M. Smeulders, and H. Geerts. Robust autofocusing in microscopy. *Cytometry*, 39(1):1–9, 2000.

[53] B. Forster, D. Van De Ville, J. Berent, D. Sage, and M Unser. Complex wavelets for extended depth-of-field: A new method for the fusion of multichannel microscopy images. *Microscopy Research and Technique*, 65(1-2):33–42, September 2004.

[54] Satoshi A. Sugimoto and Yoshiki Ichioka. Digital composition of images with increased depth of focus considering depth information. *Appl. Opt.*, 24:2076–2080, jul 1985.

[55] A.G. Valdecasasa, D. Marshallb, J.M. Becerraa, and J.J. Terreroa. On the extended depth of focus algorithms for bright field microscopy. *Micron*, 32:559–569, 2001.

[56] Paul M de Zeeuw, Eric J Pauwels, and Jungong Han. Multimodality and multiresolution image fusion. *International Conference on Computer Vision Theory and Applications*, pages 151–157, 2012.

[57] Manfred U. A. Bromba and Horst Ziegler. Application hints for savitzky-golay digital smoothing filters. *Anal. Chem.*, 53(11):1583–1586, 1981.

[58] R.N. Bracewell. *The Fourier Transform and Its Applications*. Electrical engineering series. McGraw Hill, 2000.

[59] NVIDIA Corporation. Cuda c programming guide v5.5. 2013.

[60] Nvidia Corp. Cufft library. 2013.

[61] B.E.A. Saleh and M.C. Teich. *Fundamentals of Photonics*. Wiley Series in Pure and Applied Optics. Wiley, 2007.

[62] Long Chen, Yue Wang, Nenrong Liu, Duo Lin, Cuncheng Weng, Jixue Zhang, Lihuan Zhu, Weisheng Chen, Rong Chen, and Shangyuan Feng. Near-infrared confocal micro-raman spectroscopy combined with pca–lda multivariate analysis for detection of esophageal cancer. *Laser Physics*, 23(6):065601, 2013.

[63] Bingling Chen, Shaoxin Li, Jianghua Li, Zhouyi Guo, Qiuyan Chen, and Haiqiang Mai. Optimal multivariate method for raman spectroscopy based diagnosis of nasopharyngeal carcinoma. *Journal of Applied Physics*, 114(24):244702–244702–6, Dec 2013.

[64] Li Yongzeng, Pan Jianji, Chen Guannan, Li Chao, Lin Shaojun, Shao Yonghong, Feng Shangyuan, Huang Zufang, Xie Shusen, Zeng Haishan, and Chen Rong. Micro-raman spectroscopy study of cancerous and normal nasopharyngeal tissues. *Journal of Biomedical Optics*, 18(2), 2013.

[65] Wolthuis R, Bakker Schut TC, Caspers PJ, Buschman HPJ, Romer TJ, Bruining HA, and Puppels GJ. Raman spectroscopic methods for in vitro and in vivo tissue characterization, in fluorescent and luminescent probes for biological activity, 2nd ed. *Academic Press, San Diego*, pages 433–455, 1999.

[66] F. Severcan and P.I. Haris. *Vibrational Spectroscopy in Diagnosis and Screening*, volume 6. IOS Press, June 2012.

[67] Catherine Kendall, Martin Isabelle, Florian Bazant-Hegemark, Joanne Hutchings, Linda Orr, Jaspreet Babrah, Rebecca Baker, and Nicholas Stone. Vibrational spectroscopy: a clinical tool for cancer diagnostics. *Analyst*, 134:1029–1045, 2009.

[68] JM Roberts, AM Gurley, JK Thurloe, R Bowditch, and CR Laverty. Evaluation of the thinprep pap test as an adjunct to the conventional pap smear. *The Medical journal of Australia*, 167(9):466âĂŤ469, November 1997.

[69] Ronald F Lamont, Elizabeth A Hudson, Phillip E Hay, D John Morgan, Vikash Modi, Cathy A Ison, and David Taylor-Robinson. A comparison of the use of papanicolaou-stained cervical cytological smears with gram-stained vaginal smears for the diagnosis of bacterial vaginosis in early pregnancy. *International Journal of STD and AIDS*, 10(2):93–97, 1999.

[70] G. Altmann, O. Lade, L.A. Ladic, and S. Rausch. Method for colouring cell samples for microscopy, 2014. WO Patent App. PCT/EP2014/051,761.

[71] Bolger N, Heffron C, Regan I, Sweeney M, Kinsella S, McKeown M, Creighton G, Russell J, and O'Leary J. Implementation and evaluation of a new automated interactive image analysis system. *Acta Cytol*, 483-91(50(5)), Sep. 2006.

[72] Anita Mahadevan-Jansen, Michele Follen Mitchell, Nirmala Ramanujamf, Anais Malpica, Sharon Thomsen, Urs Utzinger, and Rebecca Richards-Kortumt. Near-infrared raman spectroscopy for in vitro detection of cervical precancers. *Photochemistry and Photobiology*, 68(1):123–132, 1998.

[73] Anita Mahadevan-Jansen, Michele Follen Mitchell, Nirmala Ramanujam, Urs Utzinger, and Rebecca Richards-Kortum. Development of a fiber optic probe to measure nir raman spectra of cervical tissue in vivo. *Photochemistry and Photobiology*, 68(3):427–431, 1998.

[74] Elizabeth M. Kanter, Elizabeth Vargis, Shovan Majumder, Matthew D. Keller, Emily Woeste, Gautam G. Rao, and Anita Mahadevan-Jansen. Application of raman spectroscopy for cervical dysplasia diagnosis. *Journal of Biophotonics*, 2(1-2):81–90, 2009.

[75] American Cancer Society. Bladder cancer. pages 05–06, 2014.

[76] HG Wiener, GP Vooijs, and B van't Hof-Grootenboer. Accuracy of urinary cytology in the diagnosis of primary and recurrent bladder cancer. *Acta cytologica*, 37(2):163âĂŤ169, 1993.

[77] Felix M. Brown. {URINE} cytology: Is it still the gold standard for screening? *Urologic Clinics of North America*, 27(1):25 – 37, 2000.

[78] Laura T. Kerr, Aine Adams, Shirley O'Dea, Katarina Domijan, Ivor Cullen, and Bryan M. Hennelly. Classification of bladder cancer cell lines using raman spectroscopy: a comparison of excitation wavelength, sample substrate and statistical algorithms. *Proc. SPIE*, 9129:91290E, WA 2014.

[79] Brooke D. Beier and Andrew J. Berger. Method for automated background subtraction from raman spectra containing known contaminants. *Analyst*, 134:1198–1202, 2009.

[80] Ute B. Cappel, Ian M. Bell, and Laura K. Pickard. Removing cosmic ray features from raman map data by a refined nearest neighbor comparison method as a precursor for chemometric analysis. *Applied Spectroscopy*, 64(2):195–200, 2010-02-01.